

BIASES IN VIRIAL BLACK HOLE MASSES: AN SDSS PERSPECTIVE

YUE SHEN¹, JENNY E. GREENE^{1,2}, MICHAEL A. STRAUSS¹, GORDON T. RICHARDS³, DONALD P. SCHNEIDER⁴

Submitted to ApJ on September 19, 2007

ABSTRACT

We compile black hole (BH) masses for $\sim 60,000$ quasars in the redshift range $0.1 \lesssim z \lesssim 4.5$ included in the Fifth Data Release of the Sloan Digital Sky Survey (SDSS), using virial BH mass estimators based on the $H\beta$, $MgII$, and CIV emission lines. We find that: (1) within our sample, the widths of the three lines follow log-normal distributions, with means and dispersions that do not depend strongly on luminosity or redshift; (2) the $MgII$ - and $H\beta$ -estimated BH masses are consistent with one another; and (3) the CIV BH mass estimator may be more severely affected by a disk wind component than the $MgII$ and $H\beta$ estimators, giving a positive bias in mass correlated with the CIV - $MgII$ blueshift. Most SDSS quasars have virial BH masses in the range $10^8 - 10^{10} M_{\odot}$. There is a clear upper mass limit of $\sim 10^{10} M_{\odot}$ for active BHs at $z \gtrsim 2$, decreasing at lower redshifts. Making the reasonable assumptions that the underlying BH mass distribution decreases with mass and that the Eddington ratio distribution at fixed true BH mass has non-zero width, we show that the measured virial BH mass distribution and Eddington ratio distribution within finite luminosity bins are subject to Malmquist bias if the scatter in luminosity at fixed true BH mass is uncorrelated with the scatter in line width. Given the current versions of virial calibrations and their uncertainties, we present a model which reproduces the observed virial mass distribution, quasar luminosity function, and line width distribution of our sample; it has an underlying BH mass distribution which is a power-law with slope $\gamma_M \sim -2.6$, and a true Eddington ratio distribution at fixed BH mass which is a log-normal with mean dependent on BH mass ($\sim 10^{-1.2}$ for typical $10^8 M_{\odot}$ BHs) and with dispersion 0.4 dex. In this model, the observed virial mass distribution for the SDSS sample is biased high by ~ 0.6 dex within finite luminosity bins, and the Eddington ratio distribution is biased low by the same amount. A radio quasar subsample (with $1.5 \lesssim z \lesssim 2.3$) has mean virial BH mass larger by ~ 0.12 dex than the radio-quiet sample matched in luminosity and redshift. A broad absorption line (BAL) quasar subsample (with $1.7 \lesssim z \lesssim 2.2$) has a virial mass distribution identical to that of the non-BAL quasar sample matched in luminosity and redshift, with no mean offset.

Subject headings: black hole physics – galaxies: active – galaxies: fundamental parameters – galaxies: high-redshift – quasars: general – surveys

1. INTRODUCTION

There has been increasing interest in recent years in the role that supermassive black holes (SMBHs) play in galaxy formation, primarily because of the discovery that most, if not all, present-day massive galaxies harbor a SMBH in their nuclei (e.g., Kormendy & Richstone 1995; Richstone et al. 1998), and that the mass of the nuclear SMBH is related to the bulge mass/luminosity (e.g., Magorrian et al. 1998) and even more tightly to the bulge stellar velocity dispersion (e.g., Ferrarese & Merritt 2000; Gebhardt et al. 2000a; Tremaine et al. 2002). These tight correlations imply that the formation of galaxies and the growth of the central SMBHs are ultimately connected (e.g., Silk & Rees 1998; Kauffmann & Haehnelt 2000; Wyithe & Loeb 2003; Di Matteo et al. 2005; Hopkins et al. 2006).

On the other hand, it has long been suggested that active galactic nuclei (AGN) or quasars are SMBHs in the process of accretion and growth (e.g., Salpeter 1964; Zel'dovich & Novikov 1964; Lynden-Bell 1969). Indeed, the integrated luminosity density of optically-selected AGNs, which represents the accretion history of black holes, is consistent with the mass density in the local dormant SMBH population (the Sołtan [1982] argument; e.g., Salucci et al. 1999; Yu &

Tremaine 2002). This is particularly encouraging, since with ever larger AGN/quasar samples in modern surveys, we can hope to understand the cosmic evolution of SMBHs within the framework of hierarchical structure formation, and shed light on the coevolution of SMBHs and their host galaxies. A central issue in this regard is to measure the masses of both inactive SMBHs and active AGNs/quasars.

Perhaps the most reliable way to measure the black hole mass is via stellar/gas dynamics in the vicinity of the SMBH where its gravity dominates the dynamics (e.g., Richstone et al. 1998), but the relevant scales can be resolved only for the nearest galaxies. A more indirect mass indicator uses the observed tight correlations between the SMBH mass M_{BH} and the stellar bulge velocity dispersion σ (the $M-\sigma$ relation), or the bulge luminosity (the $M-L$ relation). Accurate measurements of the bulge velocity dispersion or bulge luminosity are difficult in luminous quasars, where the AGN light overwhelms that of the host galaxy; these relations are mostly applied to measure the local dormant SMBH mass function. More seriously, the $M-\sigma$ and $M-L$ relations have not been measured directly at the most massive end, and the high-mass end of the BH mass functions estimated using the $M-\sigma$ and $M-L$ relations differ by as much as one order of magnitude (Tundo et al. 2007; Lauer et al. 2007). Thus there are still unsettled issues on the usage of these techniques.

A third method, reliant on AGN physics rather than galaxy properties, is reverberation mapping, which uses the temporal offset between continuum and emission line variability to determine the distance R from the central engine to the broad

¹ Princeton University Observatory, Princeton, NJ 08544.

² Hubble Fellow and Princeton-Carnegie Fellow.

³ Department of Physics, Drexel University, 3141 Chestnut Street, Philadelphia, PA 19104.

⁴ Department of Astronomy and Astrophysics, 525 Davey Laboratory, Pennsylvania State University, University Park, PA 16802.

emission line region (BLR; e.g., Blandford & McKee 1982; Peterson 1993; Kaspi et al. 2000; Peterson et al. 2004). Using the observed line width V and assuming that the BLR is virialized allows determination of the black hole mass: $M_{\text{BH}} \simeq G^{-1}RV^2$. In a handful of cases, measurements of V and R for several lines in the same object have shown $V \propto R^{-1/2}$, consistent with the virial hypothesis (e.g., Peterson & Wandel 2000). Furthermore, for the few cases in which we have more than one mass indicator, the reverberation mapping mass is also consistent with the dynamical mass or that derived from the $M_{\text{BH}} - \sigma$ relation (e.g., Gebhardt et al. 2000b; Ferrarese et al. 2001; Nelson et al. 2004; Onken et al. 2004, 2007; Greene & Ho 2006; Davies et al. 2006). The reverberation mapping method is very time consuming, and we have reliable masses with this method for only about three dozen AGNs.

However, reverberation mapping data has revealed a correlation between BLR size R and luminosity (Kaspi et al. 2000, 2005), which allows us to estimate BH masses based on single-epoch spectra. Using this $R-L$ correlation and reverberation mapping masses, various empirical scaling relations (which we term virial BH mass estimators from now on) have been derived using $H\beta$ (Kaspi et al. 2000; Vestergaard 2002; McLure & Jarvis 2002; Vestergaard & Peterson 2006), $H\alpha$ (Greene & Ho 2005), MgII (McLure & Jarvis 2002; McLure & Dunlop 2004), and CIV (e.g., Vestergaard 2002; Vestergaard & Peterson 2006). This is the only practical method for measuring black hole masses for large numbers of objects at high redshifts and luminosities (where variability timescales are too long to measure easily; see the discussion in Kaspi et al. 2007), but the $R-L$ relation has only been established in the luminosity range $\sim 10^{42} - 10^{46} \text{ erg s}^{-1}$ and for redshifts $z < 0.3$.

The virial BH mass estimators are usually expressed as:

$$\log\left(\frac{M_{\text{BH, vir}}}{M_{\odot}}\right) = a + b \log\left(\frac{\lambda L_{\lambda}}{10^{44} \text{ erg s}^{-1}}\right) + 2 \log\left(\frac{\text{FWHM}}{\text{km s}^{-1}}\right), \quad (1)$$

where λL_{λ} , the surrogate for the BLR size R , is the continuum luminosity near the emission line (5100Å for $H\beta$, 3000Å for MgII and 1350Å for CIV), and FWHM is the full-width-at-half-maximum of the line. Some authors prefer to use other quantities in their virial estimates. For example, Wu et al. (2004) suggest using recombination line luminosities instead of continuum luminosities because the latter might be contaminated by jet emission or host galaxy starlight (also see Greene & Ho 2005). Peterson et al. (2004) and Collin et al. (2006) argue that the second moment of the line profile σ_{line} is a better quantity to characterize the emission-line widths than the FWHM. As we will show below, different measurement techniques yield systematic differences in derived quantities, and so it is important to use the original definitions of line widths and luminosities for whichever calibration is used.

The UV CIV virial mass estimator can be used for $z \gtrsim 2$ quasars, as the CIV line is the only relevant line available in optical spectra in this redshift range. However, it has been suggested by a few authors that the CIV line might be a less secure mass estimator than MgII or $H\beta$. The CIV line tends to be asymmetric and blueshifted with respect to lower-ionization lines such as $H\beta$ or MgII (e.g., Gaskell 1982; Tytler & Fan 1992), and the most blueshifted objects tend to have the largest FWHMs (Richards et al. 2002b). These features suggest that CIV might be more severely affected than the other lines by a non-virialized gas component, and the measured line width could depend on the viewing angle, biasing the

BH mass estimates. Indeed, using a sample of ~ 80 $z \leq 0.5$ Palomar-Green (Green, Schmidt, & Liebert 1986) quasars, Baskin & Laor (2005) showed that the CIV FWHM is poorly correlated with the $H\beta$ FWHM (e.g., see their figure 3), suggesting that the two lines have different origins. On the other hand, the MgII FWHM is well-correlated with that of $H\beta$, and these two low-ionization line estimators usually give consistent virial masses (e.g., McLure & Dunlop 2004; Salviander et al. 2007). One of the purposes of this paper is to explore how the CIV estimator might be biased relative to low-ionization line estimators such as MgII using a large sample of quasars from the Sloan Digital Sky Survey (SDSS; York et al. 2000).

Despite the caveats in these virial estimators, virial BH masses have been measured for various AGN/quasar samples covering a wide range of redshifts and luminosities. For example, McLure & Dunlop (2004) measured virial BH masses for 12698 quasars with $0.1 \leq z \leq 2.1$ from the SDSS DR1 quasar catalog (Schneider et al. 2003) using $H\beta$ and MgII . Vestergaard (2004) used $H\beta$ and CIV to measure virial BH masses for a hybrid sample including 87 $z \leq 0.5$ Bright Quasar Survey (BQS, Schmidt & Green 1983) quasars, 114 $1.5 \lesssim z \lesssim 3.5$ quasars, and ~ 150 $z > 3.5$ SDSS quasars. Greene & Ho (2007) present the BH mass function for ~ 8500 broad-line AGNs with $z < 0.35$ from the SDSS. Fine et al. (2006) used composite spectra to measure the redshift evolution of the mean BH mass for the 2QZ quasar sample (Croom et al. 2004) from $z \sim 0.5$ to $z \sim 2.5$, and Kollmeier et al. (2006) presented virial BH masses for a sample of 407 AGN with $z \sim 0.3 - 4$ selected from the AGN and Galaxy Evolution Survey (AGES; Kochanek et al. 2004) and focused on the distribution of Eddington ratios. Yet by far the largest quasar sample is the recently published SDSS DR5 quasar catalog (Schneider et al. 2007), containing more than 77,000 quasars, about half of which are homogeneously selected (e.g., Richards et al. 2006a; Shen et al. 2007). In this paper we present virial BH mass estimates for this optical quasar sample and explore possible biases in their estimation. Though the dynamical range in luminosity and color of SDSS quasars is limited, the large size of the sample provides unprecedented statistics.

The paper is organized as follows: in § 2 we describe our quasar sample. We present our procedures of estimating virial BH masses in § 3, where we compare results from different lines in detail. The distributions of black hole masses and Eddington ratios are described in § 4, and we discuss our results as well as some general issues with virial estimators in § 5. We summarize our results in § 6. Throughout this paper we adopt a flat Λ CDM cosmology: $\Omega_M = 0.26$, $\Omega_{\Lambda} = 0.74$ and $h = 0.71$ (Spergel et al. 2007).

2. THE SAMPLE

The SDSS uses a dedicated 2.5-m wide-field telescope (Gunn et al. 2006) with a drift-scan camera with $30 \times 2048 \times 2048$ CCDs (Gunn et al. 1998) to image the sky in five broad bands (*ugriz*; Fukugita et al. 1996). The imaging data are taken on dark photometric nights of good seeing (Hogg et al. 2001), are calibrated photometrically (Smith et al. 2002; Ivezić et al. 2004; Tucker et al. 2006) and astrometrically (Pier et al. 2003), and object parameters are measured (Lupton et al. 2001; Stoughton et al. 2002). Quasar candidates (Richards et al. 2002a) for follow-up spectroscopy are selected from the imaging data using their colors, and are arranged in spectroscopic plates (Blanton et al. 2003) to be observed with a pair of double spectrographs. The quasars observed through

the Third Data Release (Abazajian et al. 2005) have been cataloged by Schneider et al. (2005), while Schneider et al. (2007) extend this catalog to the DR5 (Adelman-McCarthy et al. 2007a).

Our parent sample is the published SDSS DR5 quasar catalog (Schneider et al. 2007), which contains 77,429 bona fide quasars that have luminosities larger than $M_i = -22.0$ (using a slightly different cosmology in that paper) and have at least one broad emission line ($\text{FWHM} > 1000 \text{ km s}^{-1}$) or have interesting/complex absorption features. About half of the quasars in this catalog were selected from a uniform algorithm (as described in Richards et al. 2002a), which is flux limited to⁵ $i = 19.1$ at $z \lesssim 3$ and $i = 20.2$ at $z \gtrsim 3$ (magnitudes are corrected for Galactic extinction using the Schlegel, Finkbeiner & Davis 1998 map). These objects are flagged with the UNIFORM FLAG = 1 in the DR5 quasar catalog, and they can be used to construct a statistically homogeneous sample (e.g., Richards et al. 2006a; Shen et al. 2007).

There are also flags indicating whether or not a quasar is detected in the *FIRST* (Becker et al. 1995) or *ROSAT* (Voges et al. 1999) surveys, which we will use to define our radio quasar subsample (see §4.6). Most of our analysis will avoid broad absorption line quasars (BALs), whose line widths are problematic to measure; we will come back to the BALs in §4.6. We have identified ~ 4200 BALs (with $1.7 \leq z \leq 4.2$ for C IV and $0.5 \leq z \leq 1.9$ for Mg II; Shen et al. 2008) in the DR5 quasar catalog using traditional BAL criteria (Weymann et al. 1991). This list of BALs is by no means complete, and an official DR5 BAL catalog is forthcoming (Hall et al., in preparation; see Trump et al. 2006 for the DR3 BAL catalog).

All spectra are reduced with the new version of the SDSS spectroscopic reduction pipeline, as described in the DR6 paper (Adelman-McCarthy et al. 2007b); the flux scale of these spectra is higher than that of previous releases by roughly 38%. Thus in this paper all luminosities measured from spectra will be typically larger by ~ 0.14 dex than previous values for the same objects.

A comprehensive catalog of our measurements of the spectral properties of each quasar is given in the electronic version of this paper; the columns are described in Table 1. This catalog can be regarded as an extension to the published DR5 quasar catalog.

3. BLACK HOLE MASS ESTIMATES

To estimate BH masses using virial estimators one needs two parameters: the width of an emission line and the corresponding continuum luminosity. However, different authors have used different definitions of line width in their calibrations of the virial mass estimators. In what follows, we take care to define line width in a way consistent with each calibration we use. We also note that the assumed virial coefficient f , which accounts for our ignorance of the BLR geometry, is different in different calibrations. For instance, $f = 1$ in McLure & Dunlop (2004) and $f \sim 5.5$ (e.g., Onken et al. 2004) in Vestergaard & Peterson (2006). Thus different versions of calibration for the same line do not necessarily yield the same results, especially when extrapolated to high luminosity quasars. We will discuss this further in §5.1.

We focus on nonBALs throughout this section and §4.1-

⁵ There are a few $i > 19.1$ quasars at $z \lesssim 3$ which were selected by the high- z (*griz*) branch of the targeting algorithm (Richards et al. 2002b). The fraction of these objects is tiny ($\lesssim 2\%$). Although these objects have UNIFORM FLAG = 1 in Table 1, they will be rejected when constructing a flux-limited sample (see §4.3).

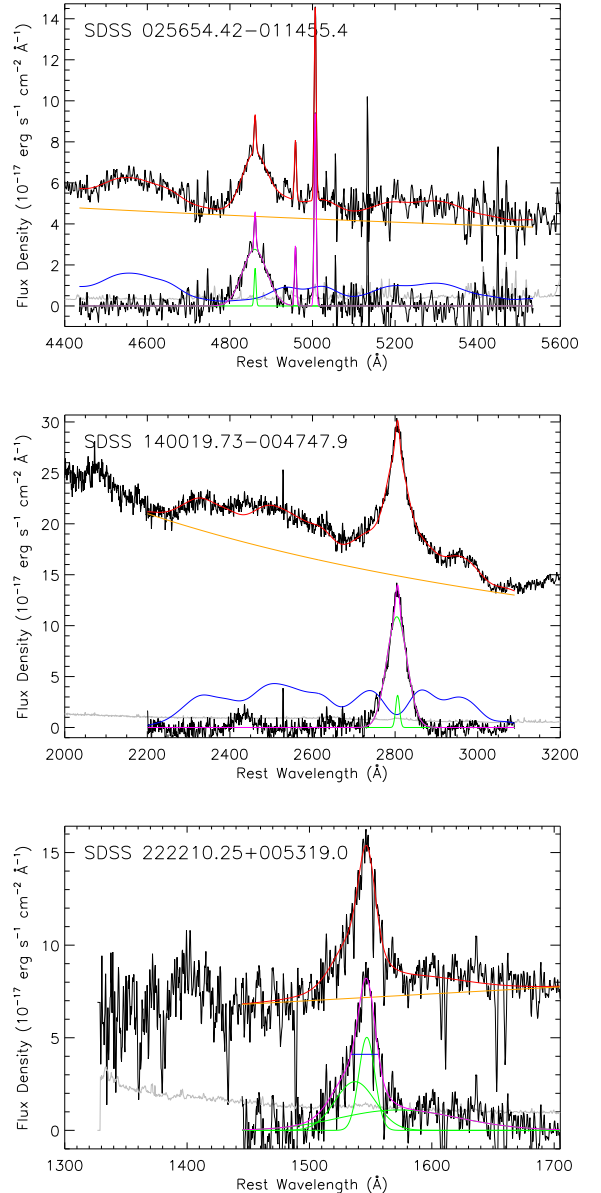


FIG. 1.— Examples of spectral fits. From top to bottom: $H\beta$, Mg II, C IV. In each panel, the upper and lower black solid lines show the original and continuum+Fe subtracted spectra; the gray lines show the flux density errors; the red lines show the full fits; the orange lines show the fitted power-law continuum; the lower blue lines in the upper and middle panels show the iron template fits; the magenta lines show the fits for the emission lines and green lines show the Gaussian components. The blue horizontal segment in the bottom panel marks the FWHM for C IV.

4.5 because of the ambiguities of line width measurement for BALs; we return to the issue of BALs in §4.6.

3.1. Line widths and continuum luminosities

3.1.1. $H\beta$ and Mg II

For the $H\beta$ and Mg II estimators, we have adopted the calibrations in McLure & Dunlop (2004), hence $a = 0.672$, $b = 0.61$ for $H\beta$ and $a = 0.505$, $b = 0.62$ for Mg II in equation (1). The $H\beta$ estimator has been calibrated directly with reverberation mapping, while the $R_{\text{BLR}} - \lambda L_{\lambda}$ relation for Mg II at 3000\AA is empirically determined in McLure & Jarvis (2002) based on $H\beta$ reverberation mapping masses. We note that the calibration for Mg II in McLure & Dunlop (2004) is an up-

TABLE 1
 CATALOG FORMAT

Column	Format	Description
1	A18	SDSS DR5 designation hhmmss.ss+ddmmss.s (J2000.0)
2	F11.6	Right ascension in decimal degrees (J2000.0)
3	F11.6	Declination in decimal degrees (J2000.0)
4	F7.4	Redshift
5	F8.3	$M_i(z=2)$ ($h=0.71$, $\Omega_M=0.26$, $\Omega_\Lambda=0.74$, K -corrected to $z=2$, following Richards et al. 2006a)
6	F7.3	Bolometric luminosity ($\log(L_{\text{bol}}/\text{erg s}^{-1})$)
7	I5	Spectroscopic plate number
8	I5	Spectroscopic fiber number
9	I6	MJD of spectroscopic observation
10	I12	Target selection flag when the spectrum was taken (i.e., using TARGET photometry)
11	I3	<i>FIRST</i> selection flag (0 or 1)
12	I3	<i>ROSAT</i> selection flag (0 or 1)
13	I3	Uniform selection flag (0 or 1)
14	I3	BAL flag (0 or 1)
15	I7	$H\beta$ FWHM (km s^{-1})
16	F8.3	Monochromatic luminosity λL_λ at 5100\AA ($10^{44} \text{ erg s}^{-1}$)
17	F7.3	Virial BH mass estimated using $H\beta$ ($\log(M_{\text{BH,vir}}/M_\odot)$)
18	I7	MgII FWHM (km s^{-1})
19	F8.3	Monochromatic luminosity λL_λ at 3000\AA ($10^{44} \text{ erg s}^{-1}$)
20	F7.3	Virial BH mass estimated using MgII ($\log(M_{\text{BH,vir}}/M_\odot)$)
21	I7	CIV FWHM (km s^{-1})
22	F8.3	Monochromatic luminosity λL_λ at 1350\AA ($10^{44} \text{ erg s}^{-1}$)
23	F7.3	Virial BH mass estimated using CIV ($\log(M_{\text{BH,vir}}/M_\odot)$)
24	F7.3	Virial BH mass (using $H\beta$ for $z < 0.7$; MgII for $0.7 < z < 1.9$ and CIV for $z > 1.9$)
25	I7	CIV-MgII blueshift (km s^{-1})
26	F8.3	Mean spectrum S/N (signal-to-noise ratio)

NOTE. — (1) Objects in this table are in the same order as in the DR5 quasar catalog (Schneider et al. 2007); (2) K -corrections are the same as in Richards et al. (2006a); (3) Bolometric luminosities are computed using bolometric corrections in Richards et al. (2006b) using one of the 5100\AA , 3000\AA , or 1350\AA monochromatic luminosities depending on redshift; (4) Entries reading -9999 for FWHM, luminosity, BH mass or CIV-MgII blueshift measurement indicate that this quantity was not measureable from the SDSS spectrum, either because it fell outside of the SDSS spectral coverage or because of low S/N.

dated version of that in McLure & Jarvis (2002), where in the former only objects with $10^{44} \text{ erg s}^{-1} < \lambda L_\lambda < 10^{47} \text{ erg s}^{-1}$ were included in their fitting. This luminosity range is suitable for the SDSS quasar sample studied here.

We follow McLure & Dunlop (2004, Appendix A) to measure the line FWHM for $H\beta$ and MgII with slight changes in details:

- 1) a power-law continuum and an iron emission line template are simultaneously fitted to the spectrum with the $H\beta$ or MgII emission line regions excluded. The fitting ranges are $[4435,4700]\text{\AA}$ and $[5100,5535]\text{\AA}$ for $H\beta$, $[2200,2675]\text{\AA}$ and $[2925,3090]\text{\AA}$ for MgII. The iron template for $H\beta$ is taken from Boroson & Green (1992) and the iron template for MgII is a modified version of the Vestergaard & Wilkes (2001) template (Salviander et al. 2007) which extends under the MgII line itself. In the fitting, the normalization and velocity broadening of the iron template are left as free parameters.
- 2) The best-fit continuum and iron emission are then subtracted from the spectrum, and two Gaussians are fitted to each emission line, one for the broad line component and the other for the narrow line component. The line fitting ranges are $[4700,5100]\text{\AA}$ for $H\beta$ and $[2700,2900]\text{\AA}$ for MgII. The FWHM of the narrow component is constrained to be less than 1200 km s^{-1} , and that of the broad component is constrained to be larger than 1200 km s^{-1} (e.g., Hao et al. 2005). In the case of $H\beta$, two additional Gaussians whose FWHMs are tied to that of the narrow $H\beta$ component are fitted simultaneously for [OIII] 4959\AA and [OIII] 5007\AA .

The FWHM of the broad Gaussian-component of $H\beta$ and MgII is then taken as the line width to be inserted in equation (1).

It is not entirely clear if there exists a strong narrow line component for MgII, thus the way to measure the MgII FWHM in McLure & Dunlop (2004) and here is not justified. If we measure the MgII FWHM from the two-Gaussian fitted flux, it will typically be smaller by ~ 0.15 dex. However, in order to use their calibration we have to follow the same procedure to measure the MgII FWHM. As we will see later in §3.3.1, the fitted broad line FWHMs for MgII and $H\beta$ are quite similar, and as a result, both line estimators yield consistent virial masses.

For continuum luminosities λL_λ at 5100\AA for $H\beta$ and at 3000\AA for MgII, we have used the fitted continuum flux density at the corresponding wavelength and corrected for Galactic extinction using the Schlegel, Finkbeiner & Davis (1998) map.

The calibration of the $H\beta$ mass estimator is not unique, and other authors have determined slightly different versions (e.g., Vestergaard 2002; Vestergaard & Peterson 2006). We find other forms of the $H\beta$ estimator yield comparable but not identical results. In particular, the Vestergaard & Peterson (2006) $H\beta$ calibration gives a systematic ~ 0.15 dex offset compared with the McLure & Dunlop (2004) calibration. We will come back to this point in §5.

3.1.2. CIV

For the CIV estimator, we use the calibration in Vestergaard & Peterson (2006), which has $a = 0.66$ and $b = 0.53$ in equation (1).

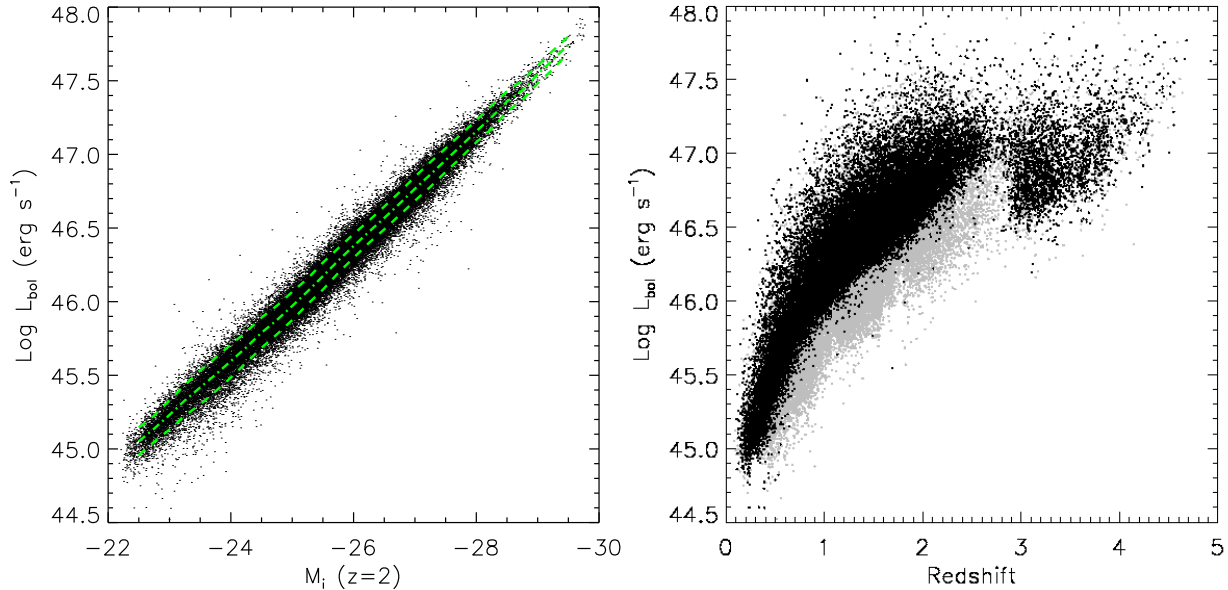


FIG. 2.— *Left*: correspondence between $M_i(z=2)$ and L_{bol} . Lines show median values and standard deviations. The absolute magnitude has been K-corrected to the i -band measured at $z=2$ (i.e., a rest-frame wavelength of $\sim 2500 \text{ \AA}$), following Richards et al. (2006a). *Right*: redshift distribution of L_{bol} for our sample, where black points are uniformly selected quasars while gray points are quasars selected with special targeting algorithms.

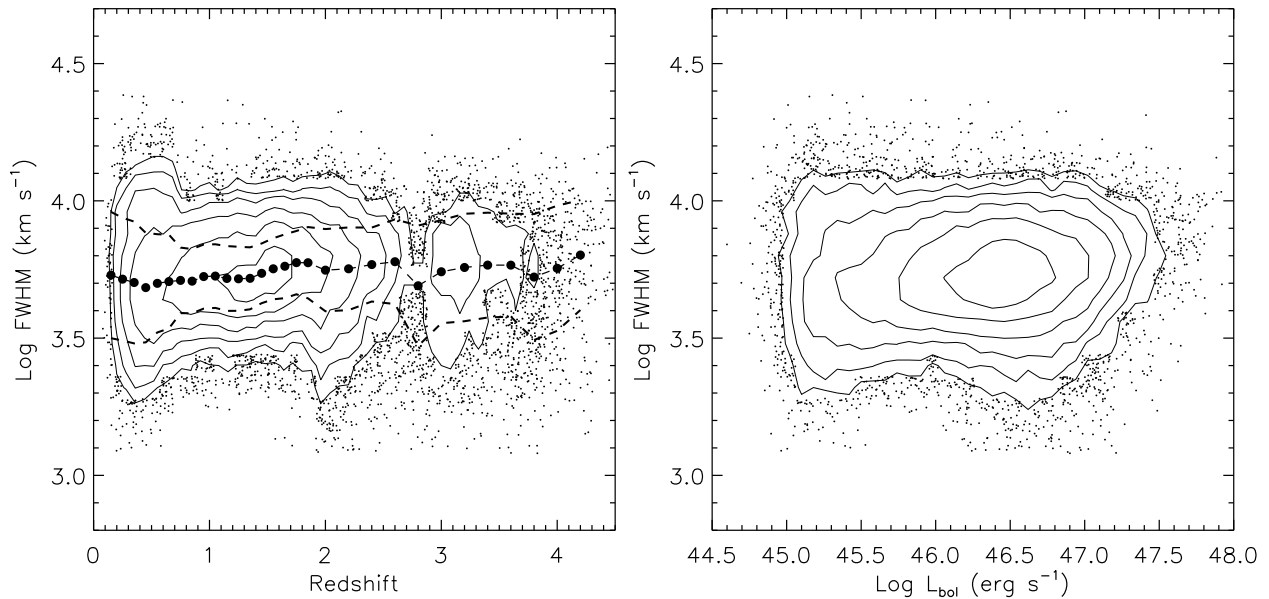


FIG. 3.— Distributions of FWHMs as functions of redshift and luminosity. The FWHMs for the three lines are plotted together. Contours are local point density contours, drawn to guide the eye. In the left panel, we also show the mean and $1-\sigma$ of the FWHM distribution as a function of redshift. FWHMs show little or no dependence on either redshift or luminosity, and their distributions follow a log-normal at all redshifts and luminosities (see Fig. 4).

Iron emission contamination is not a problem for C_{IV}, so we have simply fitted a power law continuum to regions in the vicinity of C_{IV}, namely [1445,1465]Å and [1700,1705]Å. This continuum is then subtracted from the spectrum for the line fitting which follows.

The FWHM for C_{IV} as defined in Vestergaard & Peterson (2006) is indeed the “full-width-at-half maximum” of the full line profile, whether or not the line profile is Gaussian. Since many C_{IV} lines have profiles “peakier” than a Gaussian, the FWHM obtained from a single Gaussian fit overestimates its formal definition. For this reason, following the standard approach in the literature (e.g., Baskin & Laor 2005; Fine et al. 2006), we use a set of three Gaussians to fit the C_{IV} line re-

gion [1500,1600]Å. The FWHM is then measured from the fitted model flux, providing better measurements of FWHM for noisy spectra. The C_{IV} line in high redshift quasars may be biased by associated absorption lines. To reduce their effect, a second line fit is performed which excludes pixels that are 1.5σ below the first fitted model, where σ is the estimated error in flux density. The model is replaced by the second fit if the reduced χ^2 is smaller than in the first fit. Also, if one or two of the three Gaussians have integrated flux less than 5% of the total model flux, they are removed from the model flux; this step ensures that there are no unphysically narrow peaks to bias the FWHM measurement. As in the cases of H β and MgII, we require $\text{FWHM} > 1200 \text{ km s}^{-1}$.

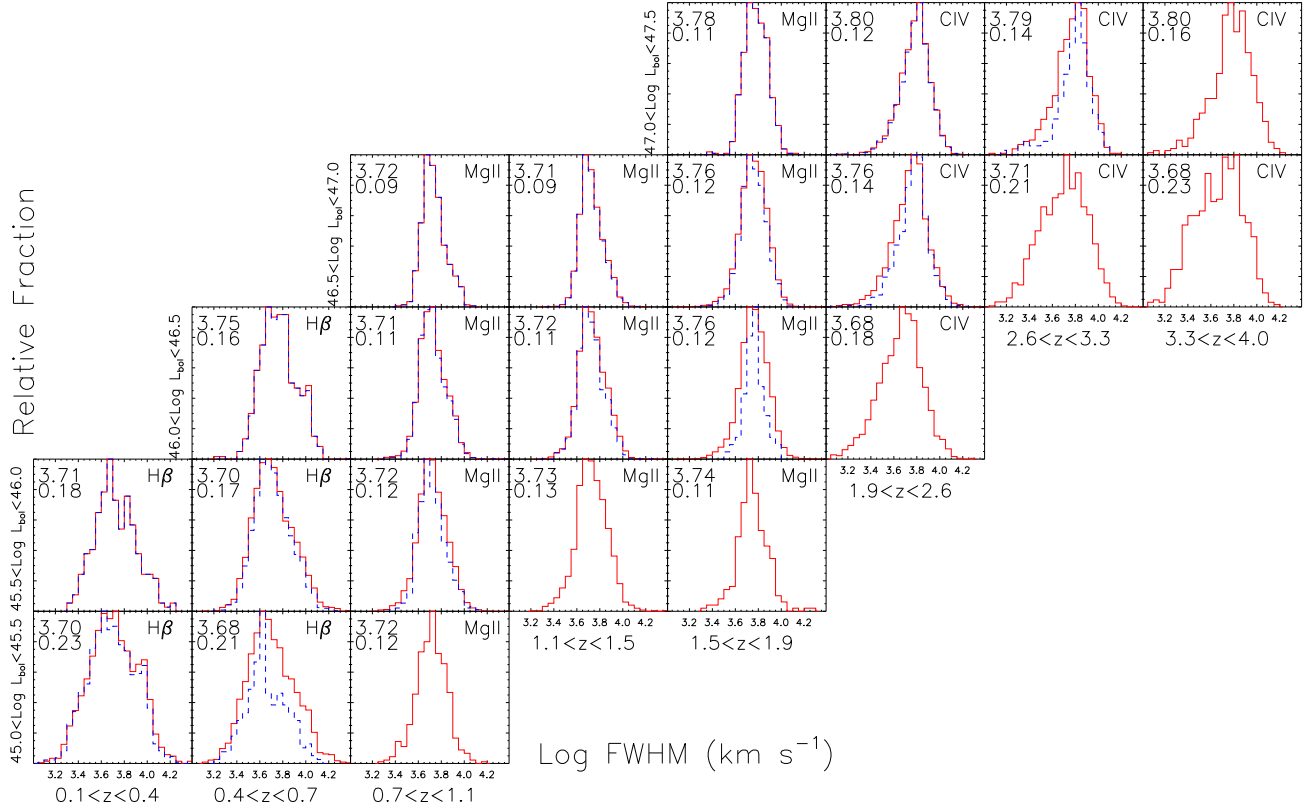


FIG. 4.— Distributions of log FWHM (in km s^{-1}) in different redshift (horizontally arranged) and luminosity (vertically arranged) bins for $\text{H}\beta$, MgII and CIV . Solid histograms show the results without a S/N cut and dashed histograms show the results with $\text{S/N} > 10$. We only plot a histogram if there are more than 200 objects (no S/N cut) or 50 objects (with S/N cut) in each bin. The number of quasars drops rapidly when we impose the S/N cut, but the solid and dashed histograms show almost identical distributions. The means and dispersions of a fitted log-normal to the distributions are shown in the upper-left corners of each panel.

The CIV FWHMs measured in this way are systematically narrower by ~ 0.15 dex than what results from a single Gaussian fit. Clearly, we would get systematic offsets in the CIV based BH masses if we used the single Gaussian FWHM.

The 1350\AA continuum luminosity λL_λ is measured using the mean flux density within the wavelength range $[1340, 1360]\text{\AA}$, and corrected for Galactic extinction. Given the wavelength coverage of the SDSS spectra, this implies that we cannot estimate CIV black hole masses for quasars with redshift below $z \sim 1.8$.

3.2. Bolometric Luminosities

For each object in our sample that has a measurable virial mass, we use its continuum luminosity λL_λ (at 1350\AA for CIV , 3000\AA for MgII and 5100\AA for $\text{H}\beta$) to estimate the bolometric luminosity. The bolometric correction factors (BC) are computed using the composite SED for a sample of SDSS-DR3 quasars constructed by Richards et al. (2006b), and are slightly different from the commonly adopted values in Elvis et al. (1994). In particular, $\text{BC}_{1350} = 3.81$, $\text{BC}_{3000} = 5.15$, $\text{BC}_{5100} = 9.26$. When two continuum luminosities are available, they give quite similar bolometric luminosities. The typical error in bolometric corrections assuming a universal SED is ~ 0.1 dex for optically-selected SDSS quasars (Richards et al. 2006b), but it might be slightly larger for BC_{1350} . The left panel of Fig. 2 shows the relation between L_{bol} and the $z = 2$ i -band absolute magnitude calculated using the K -correction in Richards et al. (2006a), while the right panel shows L_{bol} versus redshift for our sample (the darker points are the uniformly selected subsample).

Fig. 3 shows the distribution of log FWHM in bins of redshift and bolometric luminosity. The FWHMs of all three emission lines are only weakly dependent on either redshift or luminosity within our sample, and they follow a log-normal distribution with typical dispersion $\sim 0.1 - 0.2$ dex. This width is real and is not dominated by noise; we find essentially identical distributions when restricting our sample to objects with S/N per pixel greater than 10, or greater than 20. To further demonstrate that the FWHM distributions do not evolve, Fig. 4 shows the FWHM distributions for the three lines in different redshift and luminosity bins. Our measured distributions of FWHMs are consistent with other investigations (e.g., Baskin & Laor 2005; Salvander et al. 2007), with similar widths and a ~ 0.1 dex difference in the mean values⁶ (which might be caused by small differences in the techniques to determine FWHMs). The observed distribution of FWHMs has profound effects on our determination of the distribution of virial BH masses, as will be further explored in section 4.3.

3.3. Comparison of Emission Lines

There are subsamples of quasars for which we have two lines available; given the SDSS spectroscopic coverage, we observe both $\text{H}\beta$ and MgII for $0.4 \lesssim z \lesssim 0.9$, and both MgII and CIV for $1.7 \lesssim z \lesssim 2.2$. Therefore we can check if different BH mass estimators give consistent results.

3.3.1. $\text{H}\beta$ vs MgII

⁶ The difference of ~ 0.1 dex in FWHM will result in ~ 0.2 dex mean offset in virial masses. We do not consider this substantial, since the zero-point of the virial calibrations has uncertainties of the same level.

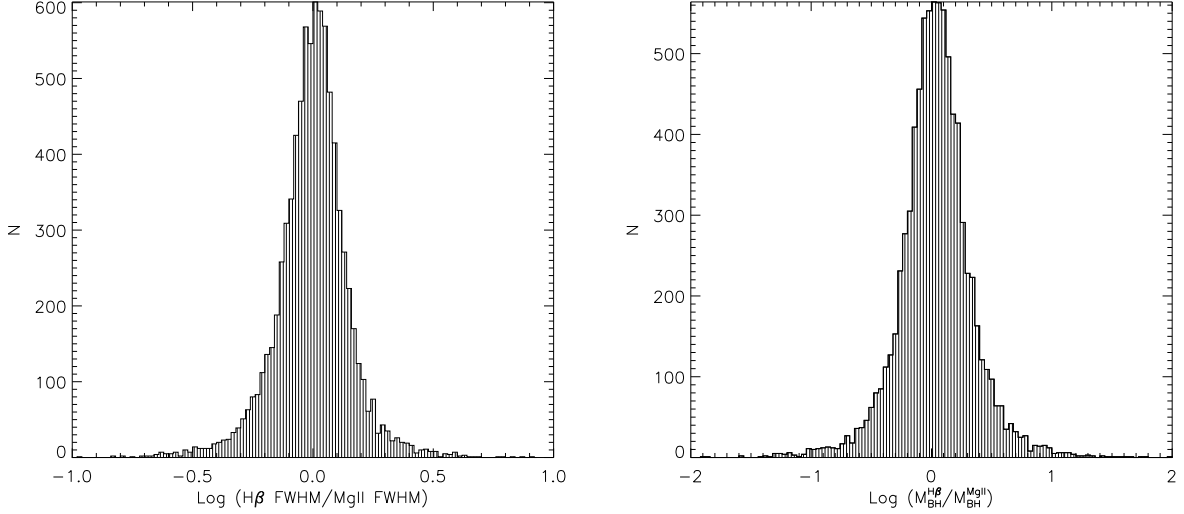


FIG. 5.— Comparisons between the $H\beta$ and the $MgII$ estimators. *left*: histogram of the FWHM ratios. *right*: histogram of the virial BH mass ratios.

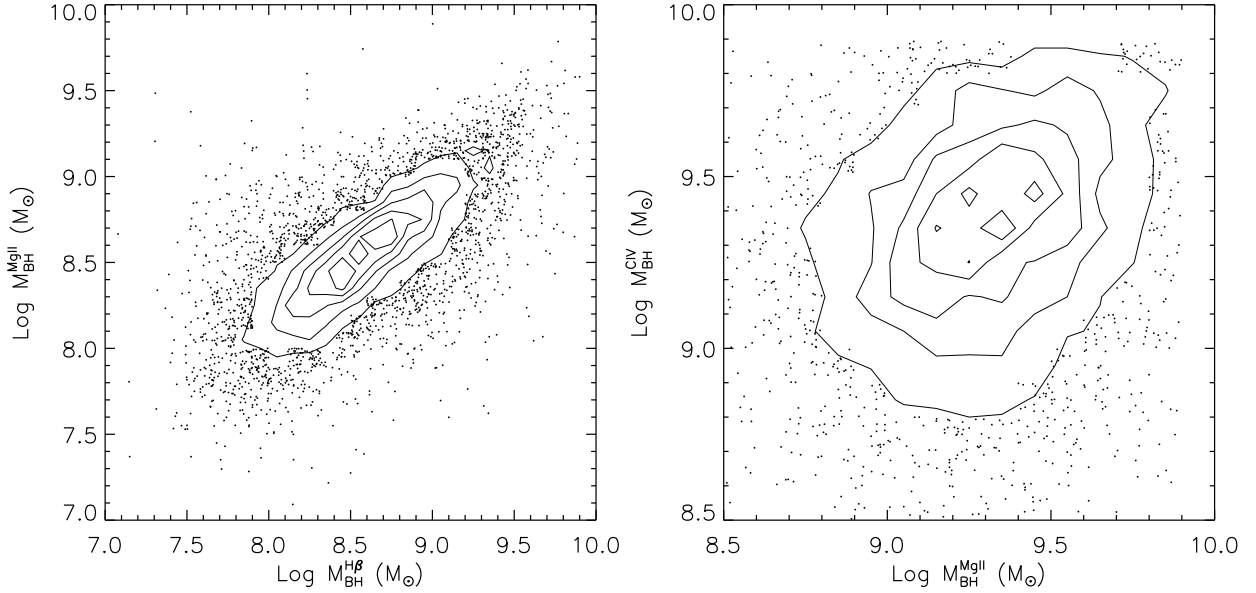


FIG. 6.— A one-to-one comparison between two virial mass estimators. *left*: $H\beta$ versus $MgII$; *right*: $MgII$ versus CIV . The correlation is much better between $H\beta$ and $MgII$ than the one between $MgII$ and CIV . Contours are local point density contours, drawn to guide the eye.

For a subsample of $\sim 8,000$ quasars with redshift $0.4 \lesssim z \lesssim 0.9$ we have both $H\beta$ and $MgII$ linewidth measurements. The distribution of $\log(H\beta \text{ FWHM}/MgII \text{ FWHM})$ is shown in the left panel of Fig. 5, which follows a Gaussian with mean 0.0062 and dispersion 0.11 dex. The distribution of $\log(M_{BH}^{H\beta}/M_{BH}^{MgII})$ is shown in the right panel of Fig. 5, which follows a Gaussian with mean 0.034 and dispersion 0.22 dex. The small discrepancy in the mean offsets between our results and those in McLure & Dunlop (2004, where the mean FWHM ratio and BH mass ratio offsets are -0.004 and 0.013 dex, respectively) is perhaps due to different samples, but is totally negligible considering the ~ 0.3 – 0.4 dex uncertainties of either of the BH mass estimators. Therefore, the $MgII$ and $H\beta$ estimators give consistent BH masses.

A plot of the $H\beta$ FWHM against the $MgII$ FWHM is very similar to Fig. 3 in Salviander et al. (2007); the two FWHMs are correlated, with a slope differing slightly from unity.

We plot the $H\beta$ against the $MgII$ virial masses in the left-hand panel of Figure 6. The two mass estimators correlate strongly with one other over two orders of magnitude in mass.

3.3.2. $MgII$ vs CIV

Linewidths of both $MgII$ and CIV are available for a subsample of $\sim 15,000$ quasars with redshift $1.7 \lesssim z \lesssim 2.2$, of which $\sim 5,000$ quasars have both $MgII$ and CIV virial masses available. However, before we compare the results, we review some of the unique characteristics of the CIV line.

First, the definitions of FWHM are quite different for $MgII$ and CIV . While the broad component of $MgII$ is well-described as a Gaussian in our fits, the vast majority of CIV lines are by no means Gaussian. The difference in line shapes suggests that the broad $MgII$ and CIV might have different physical origins. Second, it is well known that high ionization lines such as CIV often show systematic blueshifts with re-

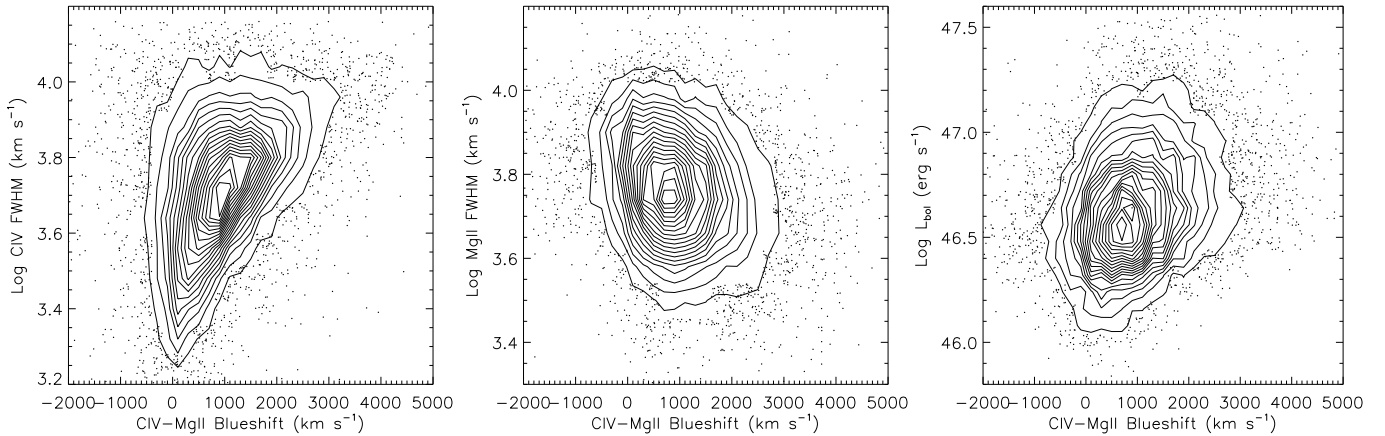


FIG. 7.— Various properties against the CIV-MgII blueshift. Contours are local point density contours, drawn to guide the eye. *Left*: CIV FWHM against blueshift. The mean value of FWHMs rises with increasing blueshift. For those objects with the largest blueshift, their FWHMs rarely drop below 4000 km s^{-1} . *Middle*: MgII FWHM against blueshift. In contrary to the CIV case, the MgII FWHM shows a mild decrease with increasing blueshift, but it is also consistent with no correlation at all considering the huge scatter. *Right*: Bolometric luminosity against blueshift. The mean luminosity increases with blueshift, but again the dispersion is large.

spect to low ionization lines such as MgII (e.g., Gaskell 1982; Tytler & Fan 1992; Richards et al. 2002b). Richards et al. (2002b) used ~ 800 SDSS quasars to show that CIV is systematically blueshifted with respect to MgII by $\sim 900 \text{ km s}^{-1}$ on average. They interpreted this apparent blueshift as due to the absorption of the CIV red wing, as might be expected if the broad-line region gas is actually a radiatively driven, equatorial outflow. Such disk-wind models are compelling for a variety of reasons, particularly their success in explaining the properties of broad absorption line quasars (e.g., Murray et al. 1995; Proga et al. 2000; Elvis 2000). Richards et al. also see a trend of increasing average CIV FWHM with increasing CIV-MgII blueshift, which again suggests that the broad CIV line is dominated by a disk wind component; in this case the CIV-MgII blueshift reflects the orientation of the line-of-sight (LOS). There is additional evidence supporting this disk wind/orientation scheme, including the anti-correlation between the CIV-MgII blueshift and radio loudness, and the correlation between the CIV-MgII blueshift and BAL fraction (see also Gallagher et al. 2005). These properties are also seen in a sample of low redshift broad line AGNs (Sulentic et al. 2007). Of course, alternative interpretations of these features are possible, which depend more on the structure of the wind than on the LOS orientation (see Richards 2006).

If the broad CIV is indeed contaminated or even dominated by a disk wind component, then the measured CIV FWHM does not represent the actual virial velocity of the BLR. If the LOS is along the disk wind, then the FWHM will overestimate the virial velocity, while if the LOS is along the pole direction, the FWHM will probably underestimate the virial velocity. Although the CIV estimator is calibrated in such a way that it gives, on average, BH masses consistent with those estimated from $H\beta$ (e.g., Vestergaard 2002; Vestergaard & Peterson 2006), there will be biases in the CIV-based virial masses if the above picture is correct.

We explore these issues by plotting various quantities against the CIV-MgII blueshift in Fig. 7. The left panel shows the correlation between the CIV FWHM and the CIV-MgII blueshift. We see the rise of the average CIV FWHM as the blueshift increases, as reported by Richards et al. (2002b). In particular, very few objects with large blueshifts have FWHM less than 4000 km s^{-1} , while the distribution of FWHM is broader for objects with small blueshifts. The middle panel

shows a mild anti-correlation between the MgII FWHM and the CIV-MgII blueshift, and the right panel shows a mild correlation between the bolometric luminosity L_{bol} and the blueshift, which has been found before (e.g., Richards et al. 2002b). The cause of the anti-correlation between MgII FWHM and CIV-MgII blueshift is not clear at this point. It might reflect inclination effects as well. The different correlations of the CIV and MgII line widths with blueshift suggest that the two lines have different origins, as we argued above.

Since the CIV estimator is calibrated using $H\beta$ reverberation mapping masses (e.g., Vestergaard 2002; Vestergaard & Peterson 2006), there should be no mean offset in either the FWHMs or the estimated BH masses, as we find (see the black solid histograms in the bottom panels in Figs. 8 and 9). While the log of the ratio of MgII to CIV FWHMs follows a Gaussian with mean 0.027 and dispersion 0.18 dex, the correlation between the two line widths is very weak (top panel of Fig. 8); indeed the width of 0.18 dex is larger than the dispersion in the MgII FWHM distribution itself. Correspondingly, the log of the ratio of MgII to CIV BH masses follows a Gaussian with mean -0.06 dex and dispersion 0.34 dex. Baskin & Laor (2005) similarly found weak correlations between the CIV and $H\beta$ FWHMs at low redshift, while Netzer et al. (2007) report a similar effect at $z \approx 2$ (but see Kelly & Bechtold 2007 for an alternate view). Moreover, this scatter is systematic with blueshift. The blue points and histogram in Figure 8 refer to objects with blueshift larger than 1000 km s^{-1} , while the red points have smaller blueshift.

The CIV and MgII virial mass estimators are plotted against one another in the right-hand panel of Figure 6. The correlation is much weaker than we found for the MgII- $H\beta$ comparison. The ratio of these two masses is correlated with the CIV-MgII blueshift, as is shown in Fig. 9 (top panel). Given the similarity between the properties of the MgII and $H\beta$ lines, and the evidence that the CIV line may be affected by a disk wind, we argue that $H\beta$ and MgII are better BH mass estimators than is CIV. In particular, we emphasize the danger of using CIV as a BH mass estimator for individual objects and small samples. For example, Kurk et al. (2007) and Jiang et al. (2007a) have obtained observations of both MgII and CIV in four $z \sim 6$ quasars. In the three quasars in which CIV-MgII blueshifts are observed, the CIV virial mass is ~ 2 times larger than the MgII mass, while they are in good agreement

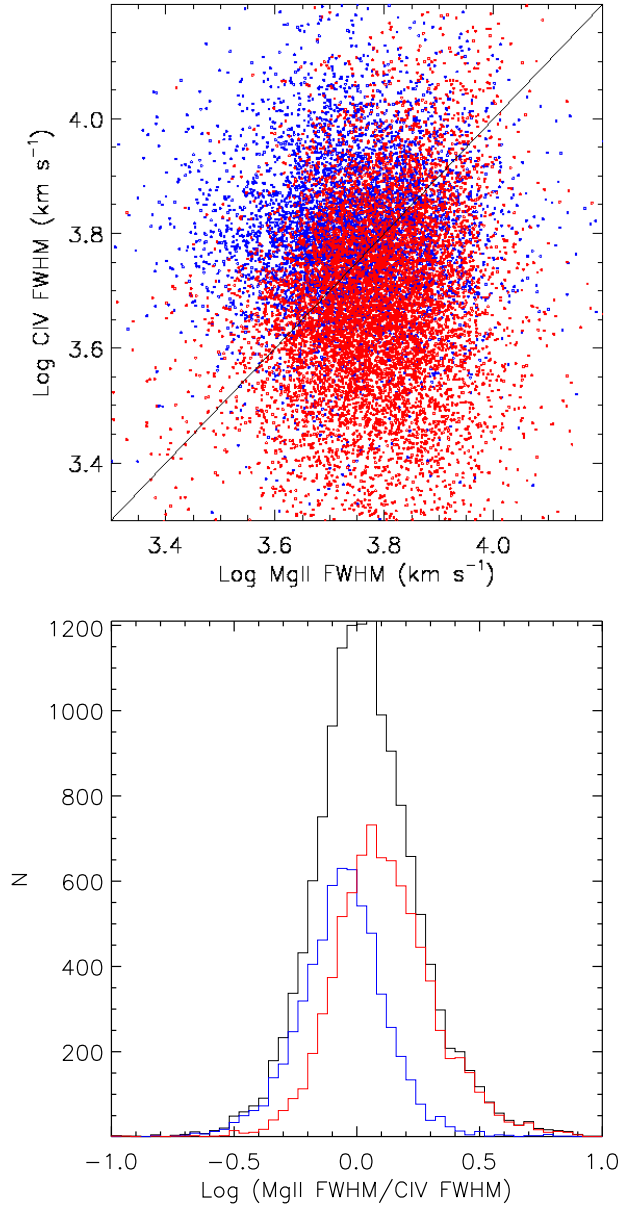


FIG. 8.— *Top*: CIV FWHMs against MgII FWHMs for a sample of quasars with both FWHMs available. Blue and red dots show those with CIV-MgII blueshift greater and less than 1000 km s^{-1} ; the solid line shows the unity relation. *Bottom*: histograms of the ratios of the MgII FWHM to the CIV FWHM. Black histogram is for the whole sample; blue and red ones are for objects with CIV-MgII blueshift greater and less than 1000 km s^{-1} .

for the one object with a CIV-MgII redshift, consistent with the trends we see in Figure 9. Finally we point out that the ratio of MgII and CIV virial masses does not depend on luminosity in the range where both line estimators are available, excluding luminosity-based biases.

Of course we cannot measure the blueshift, and thereby correct the CIV mass estimate for the bias of Figure 9, of objects for which our spectral coverage only includes CIV. However, Richards et al. (2002b) show that the CIV-MgII blueshift correlates broadly with the CIV line asymmetry, suggesting that we might use this asymmetry as a surrogate to estimate the mass estimate bias. However, the correlation between the CIV-MgII blueshift and the CIV line asymmetry shows a large amount of scatter, making it difficult to correct for this bias using the CIV line asymmetry.

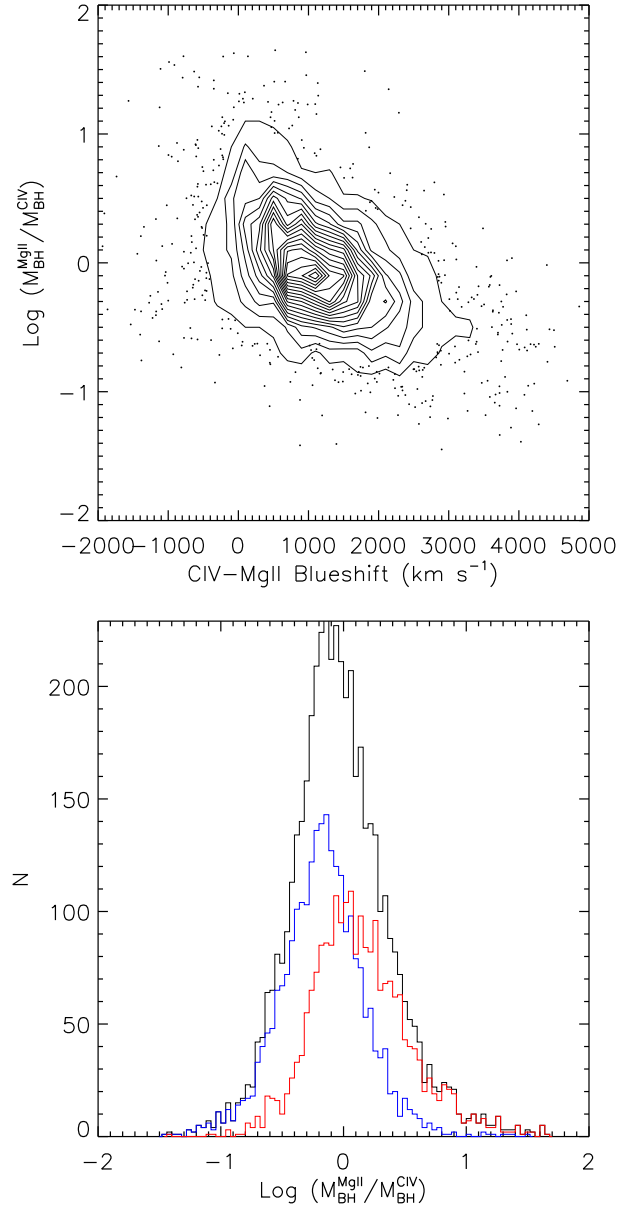


FIG. 9.— *Top*: Difference in the MgII and CIV based virial BH masses as function of the CIV-MgII blueshift. For those with small (large) blueshifts, the CIV estimator systematically underestimates (overestimates) the BH mass as compared to the MgII based virial masses. Contours are local point density contours, drawn to guide the eye. *Bottom*: Distributions of the ratios of the two virial mass estimates. The black histogram is for the entire sample; blue and red ones are for objects with CIV-MgII blueshift greater and less than 1000 km s^{-1} .

It is beyond the scope of this paper to carry out a thorough investigation of the BLR and disk geometry and dynamics needed to understand the physics behind the trends we've found. Therefore, in the following sections, we simply use the CIV estimator to measure BH masses at $z > 1.9$. Our confidence in the CIV estimator is built on the large sample studied here and the belief that there is no systematic offsets *in the mean* using the CIV estimator.

4. DISTRIBUTION OF BLACK HOLE MASSES

We present virial BH masses for the SDSS DR5 quasars with $z \lesssim 4.5$. Excluding those objects for which we cannot obtain reliable FWHM or continuum luminosity measurements due to poor spectra or redshift limitations, we have 56,872

objects (nonBALs) with measurable virial BH masses. The masses are based on the $H\beta$ estimator for $z < 0.7$, $MgII$ for $0.7 < z < 1.9$, and CIV for $1.9 < z < 4.5$, to avoid using measurements which are too close to the red and blue ends of the spectra. We should note that the quasars in this catalog were not all uniformly targeted; in particular, special targeting algorithms were used to select quasar candidates to fainter magnitudes than the main quasar survey (Richards et al. 2002a). The completeness of these fainter quasars is poor. We start by neglecting this effect; we take all the quasars in the DR5 quasar catalog with measurable masses and present the redshift evolution of virial BH masses (§4.1) and Eddington ratio distributions (§4.2). We restrict ourselves to the complete subsample in §4.3 and §4.4, where we model the observed black hole mass distribution. We describe the active BH mass function in §4.5, and discuss radio-loud and BAL quasars in §4.6.

4.1. Redshift evolution of virial BH masses

Fig. 10 shows the dependence of virial BH masses on redshift, where gray dots represent individual objects and the filled circles show the mean value at each redshift. Because of the incompleteness of the sample at the faint end, the “mean” BH masses here are weighted towards high luminosity objects at all redshifts. Nevertheless, the mean BH mass increases with redshift below $z \sim 2$, and then flattens out above $z \sim 2$; the most massive BHs seem to turn off around this epoch. There is clear evidence of a limiting BH mass $\sim 3 \times 10^9 - 10^{10} M_\odot$, consistent with the conclusions of McLure & Dunlop (2004) for $z \leq 2.1$ SDSS DR1 quasars. The trend of this figure is quite similar to fig. 4 of Vestergaard (2004), except that we have filled the gaps in their figure with our much larger sample.

4.2. Distribution of Eddington ratios

The relation between virial BH mass and bolometric luminosity is shown in Fig. 11. The figure shows objects using the three virial estimators in different colors (red for $H\beta$, green for $MgII$ and blue for CIV), while the diagonal lines indicate various Eddington ratios L/L_{Edd} , where $L_{Edd} = 1.3 \times 10^{38} (M_{BH}/M_\odot) \text{ erg s}^{-1}$ is the Eddington luminosity. The vast majority of quasars in our sample are bounded by L_{Edd} and $0.01L_{Edd}$, with a geometric mean value of $\sim 0.1L_{Edd}$. We are not surprised to see that objects using these virial relations occupy a stripe in the mass-luminosity plane, with a slope $\sim b \sim 0.5$ and scatter $\sim 0.2 - 0.3$ dex around the mean. This simply reflects the fact that the FWHM distribution is almost independent on luminosity, and has a very narrow width of $\sim 0.1 - 0.15$ dex at fixed luminosity (see Fig. 4). This also explains the remarkably similar appearance of the $M_{BH} - L_{bol}$ diagram in several other investigations even though the underlying samples are quite different (e.g., Woo & Urry 2002; Kollmeier et al. 2006), simply because similar virial estimators are used to estimate BH masses, and the FWHM distributions of different samples are similar.

Fig. 12 shows the distributions of L_{bol}/L_{Edd} in five luminosity and four redshift bins. The distribution of Eddington ratios is log-normal in almost all of the bins. No appreciable redshift evolution is seen for objects with the same luminosity. The widths of the distributions are as small as ~ 0.3 dex, similar to those in Kollmeier et al. (2006). Since virial mass is approximately proportional to the square root of luminosity, the widths of the observed Eddington ratio and the virial

BH mass distributions in each luminosity/redshift bin should be comparable, as is seen. The width of the virial BH mass distributions within each luminosity/redshift bin is thus ~ 0.3 dex or less.

At face value, the very narrow widths of the virial BH mass distribution in each luminosity bin seem somewhat surprising, since many studies have quoted significantly larger scatter between single-epoch virial masses and both reverberation-mapped masses on the one hand and stellar velocity dispersions on the other. For instance, McLure & Jarvis (2002) find an rms scatter of 0.4 dex of virial $MgII$ masses around reverberation-mapping masses, while Vestergaard & Peterson (2006) find scatters of 0.3 and 0.5 dex of the CIV and $H\beta$ virial masses about the RM masses respectively. An independent estimate may be derived by comparing virial masses with stellar velocity dispersions; Greene & Ho (2006) find an rms scatter of 0.4 dex of virial $H\alpha$ masses around the expectation from the $M - \sigma$ relation. In all of these cases, it is important to remember that the objects in question are typically much less luminous (and at much lower redshift) than the quasars we study here, but these are the measurements at our disposal at the present time.

However, the observed width of the virial mass distribution within a given luminosity/redshift bin is *not* the uncertainty in the virial mass estimators themselves. Although we do not have a deterministic model for the origin of the uncertainty in the virial relations, it must result both from the imperfect relation between luminosity and BLR radius on the one hand, and from the imperfect relation between FWHM and BLR virial velocity on the other. Thus the uncertainty in the virial mass estimators comes from the uncorrelated rms scatters in both luminosity and FWHM. When we impose luminosity cuts to our sample, i.e., either by working within luminosity bins or because of the flux limits of our sample, we will artificially narrow the observed distribution of virial masses.

At the same time, if the underlying BH mass distribution is such that there are more BHs towards lower masses/lower luminosities, then more objects will scatter from low-mass bins to high than the other way around, giving rise to a Malmquist-type bias (e.g., Eddington 1913; Malmquist 1922) in the observed virial black hole mass and Eddington ratio. In the next section, we use Monte Carlo simulations to investigate the impact of luminosity cuts and Malmquist bias on our observed distributions of luminosity, line width, virial BH masses, and Eddington ratios. The results are shown in § 4.4, where we also present an analytic derivation of the Malmquist bias.

4.3. Monte Carlo simulations

We ask whether we can reproduce the observed distributions given a set of reasonable assumptions for the true underlying distributions of black hole masses and Eddington ratios. In particular, our model should be able to reproduce the observed distributions of FWHMs in each redshift-luminosity bin, and a reasonable amount of uncertainty in virial relations. Also, the model should produce a luminosity distribution consistent with the observed quasar luminosity function. Since the BH mass and Eddington ratio distributions may evolve with redshift, we consider two redshift ranges: $0.7 < z < 1.0$, where the $MgII$ estimator is used throughout, and $1.9 < z < 2.1$, where the CIV estimator is used. We only consider the subset of uniformly-selected quasars in this section, and we restrict ourselves to objects with $\log\left(\frac{L_{bol}}{\text{erg s}^{-1}}\right) >$

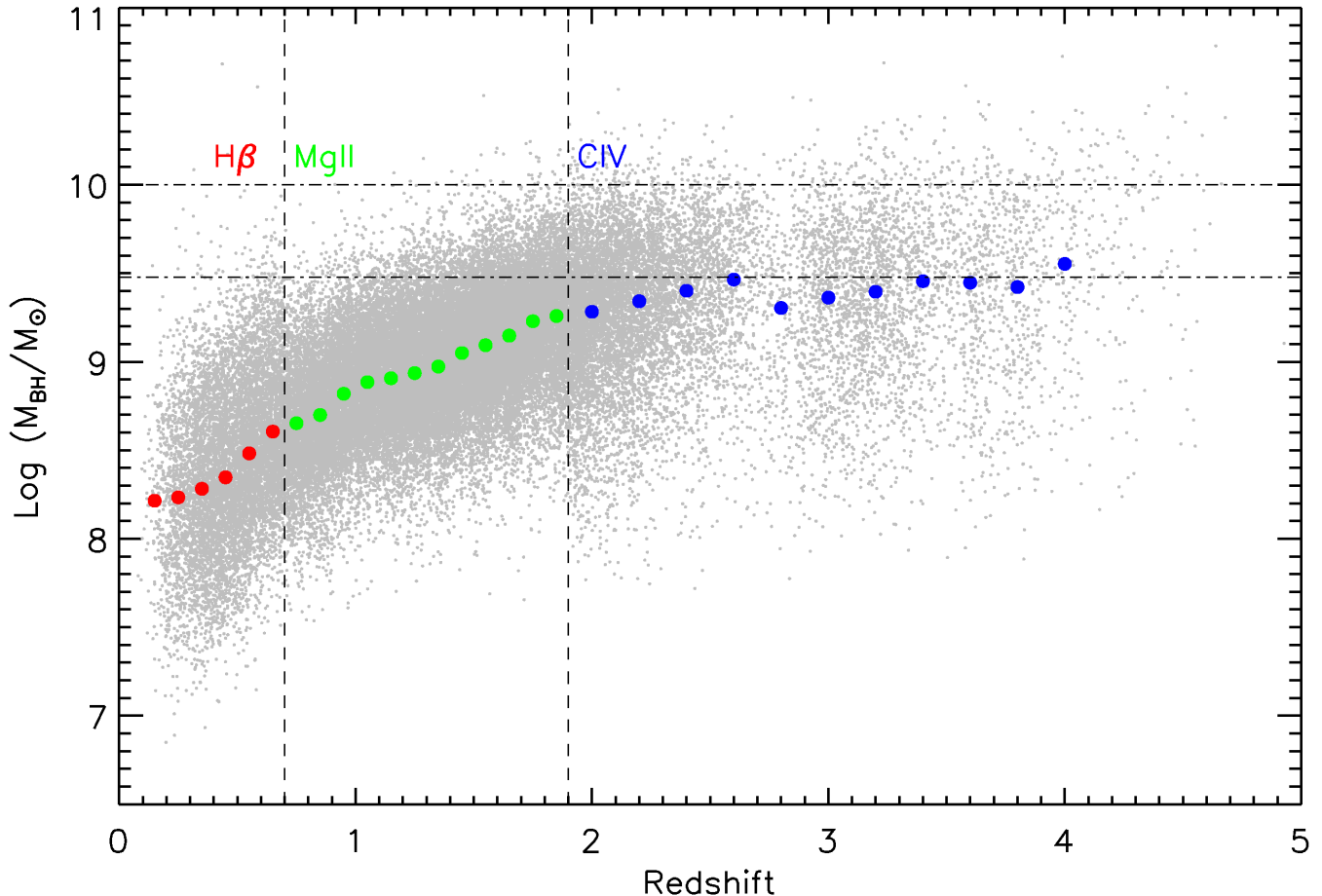


FIG. 10.— The cosmic evolution of virial BH masses for our entire DR5 quasar catalog with measurable virial masses. The two dashed vertical lines mark the transitions from one estimator to another. The filled circles show the mean value in bins of redshift of width $\Delta z = 0.1$ for $z \leq 1.9$ and $\Delta z = 0.2$ at higher redshift. The gaps around $z \sim 2.8$ and $z \sim 3.5$ are caused by the inefficiency of selecting quasars around these redshifts (e.g., Richards et al. 2002a). The upper envelope flattens out at $z \gtrsim 2$ but decreases towards lower redshift, which suggests that the most massive SMBHs are no longer shining as optical quasars at lower redshift. There is clearly an upper limit at all redshifts of black hole masses between 3×10^9 and $10^{10} M_\odot$, shown as the two dash-dotted horizontal lines.

45.9 and $\log\left(\frac{L_{\text{bol}}}{\text{erg s}^{-1}}\right) > 46.6$, respectively, above which our sample is close to complete in our two redshift ranges (e.g., Richards et al. 2006a).

In outline, we begin by specifying a model for the true black hole mass distribution. For a given mass, we will assume a single underlying central Eddington ratio (and thus bolometric luminosity) and a single underlying central FWHM. To get observed quantities (continuum luminosities and FWHM), we add scatter *independently* to the central Eddington ratio and FWHM. Our model is thus characterized by the assumed black hole mass function, the assumed relation between underlying Eddington ratios and black hole mass, and the scatters which take us to the observed luminosities and FWHM. We will present a model with reasonable (although not necessarily unique) choices for these parameters, which fits the data quite well.

The observed quasar luminosity function has a power-law form at the bright end (Richards et al. 2006a; Hopkins et al. 2007). We therefore start by assuming a power-law black hole mass distribution. For a given true black hole mass $M_{\text{BH,true}}$, we assume a central underlying Eddington ratio:

$$\left\langle \log\left(\frac{L_{\text{bol}}}{L_{\text{Edd}}}\right) \right\rangle = C_1 + C_2 \log\left(\frac{M_{\text{BH,true}}}{M_\odot}\right), \quad (2)$$

where C_1 and C_2 are constants to be set by the model. Given this Eddington ratio and our fiducial bolometric correction,

we can determine a central continuum luminosity. Given this luminosity and the true black hole mass, we *assume* that the virial estimator, equation (1), with the observed values of a and b appropriate for the sample we’re simulating, holds exactly for the central value of FWHM. That is, this central FWHM is given by:

$$\left\langle \log\left(\frac{\text{FWHM}}{\text{km s}^{-1}}\right) \right\rangle = \frac{1}{2} \left[\log\left(\frac{M_{\text{BH,true}}}{M_\odot}\right) - a - b \left\langle \log\left(\frac{\lambda L_\lambda}{10^{44} \text{ erg s}^{-1}}\right) \right\rangle \right]. \quad (3)$$

This does not give us observed quantities yet. To go from the central to *observed* bolometric and continuum luminosities, we add a scatter to each simulated object selected from a log-normal distribution of width σ_E , which is then also the width of the Eddington ratio distribution at this fixed true BH mass⁷. And to go from the central to the observed emission-line FWHM, we add a scatter to each simulated object selected from a log-normal distribution of width σ_{FWHM} . Given the observed quantities, we can simulate an “observed” virial black hole mass. By construction, then, at a given true mass, the observed virial mass is unbiased in the mean, and the un-

⁷ Here we have assumed that bolometric luminosity is always perfectly proportional to continuum luminosity, because this is how we determined the *observed* bolometric luminosities in previous sections.

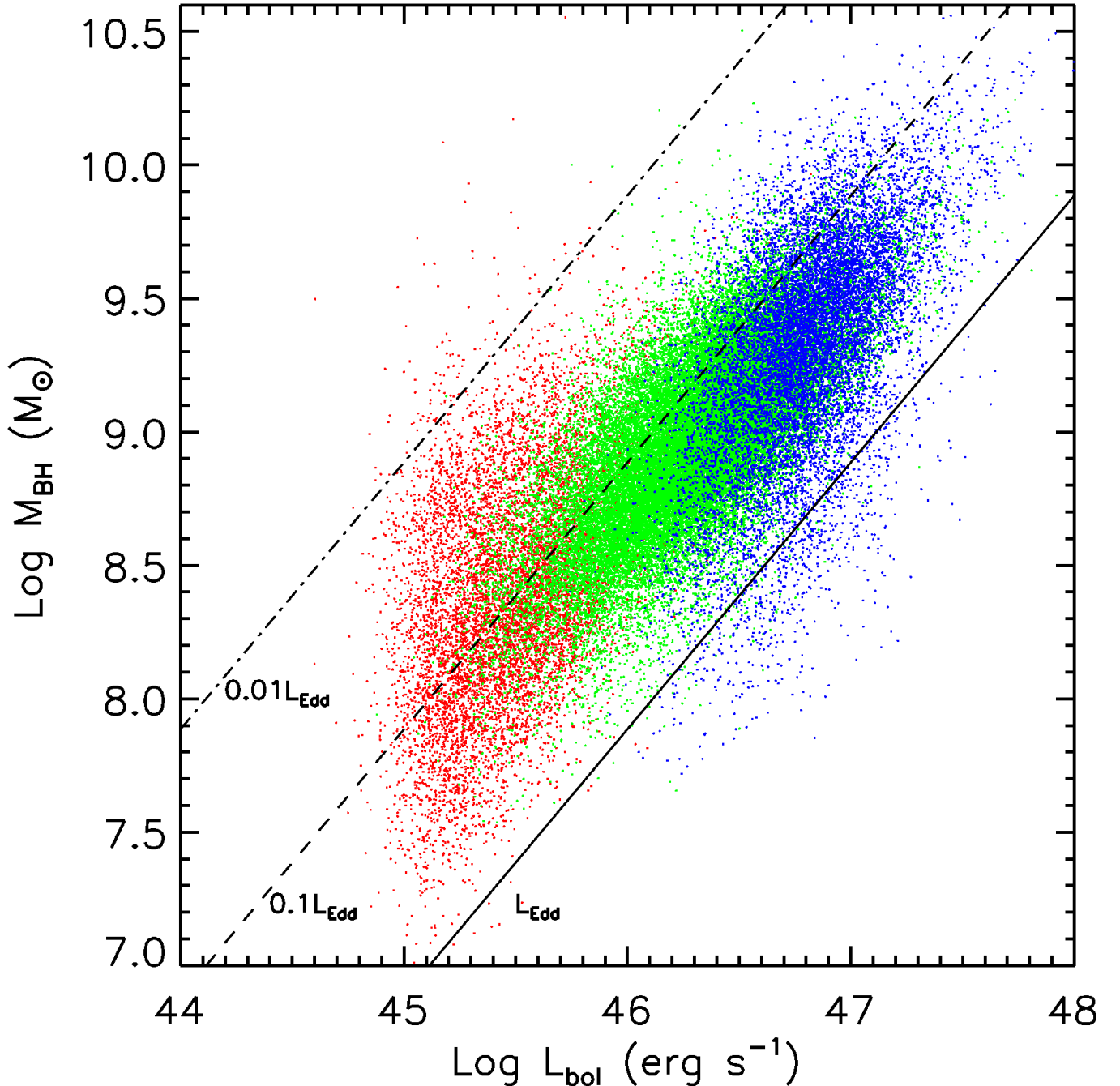


FIG. 11.— Distribution of quasars from the whole sample in the mass-luminosity diagram, where different colors show BH masses using different virial estimators (red for $H\beta$, green for $MgII$ and blue for CIV). The three diagonal lines (from top to bottom) show $0.01L_{Edd}$, $0.1L_{Edd}$ and L_{Edd} respectively. Most quasars are bounded by $L_{bol}/L_{Edd} = 0.01$ and 1 .

certainty of virial estimator at this fixed true mass is:

$$\sigma_{vir} = \sqrt{(b\sigma_E)^2 + (2\sigma_{FWHM})^2}. \quad (4)$$

The two scatters we have added, σ_E and σ_{FWHM} , are statistically independent. We discuss the physical interpretation of these scatters, the effects of any possible correlated terms, and how these quantities relate to the physical quantities of true BLR size and BLR virial velocity at fixed true BH mass, in § 5.3.

Once we have simulated luminosities for each object we can impose various luminosity cuts and make comparisons with observations. We have the freedom to vary the normalization (C_1) and mass dependence (C_2) of the central Eddington ratio

in eqn. (2), and the magnitude of the uncorrelated scatters in both FWHM (σ_{FWHM}) and Eddington ratio (σ_E), as well as the slope of the underlying power-law BH mass distribution.

The observed quasar luminosity function has a power-law form at the bright end with slope $\gamma_L \sim -2$ (Richards et al. 2006a; Hopkins et al. 2007). We therefore start by assuming a power-law BH mass function with slope γ_M . The slope of the simulated bolometric luminosity distribution will be $\sim \gamma_M/(1+C_2)$ in the limit of small σ_E , which is required to match with $\gamma_L \sim -2$. Although there is an observed break in the luminosity function (and possibly in the mass function as well), we do not include such a break in our modeling, but return to that possibility below.

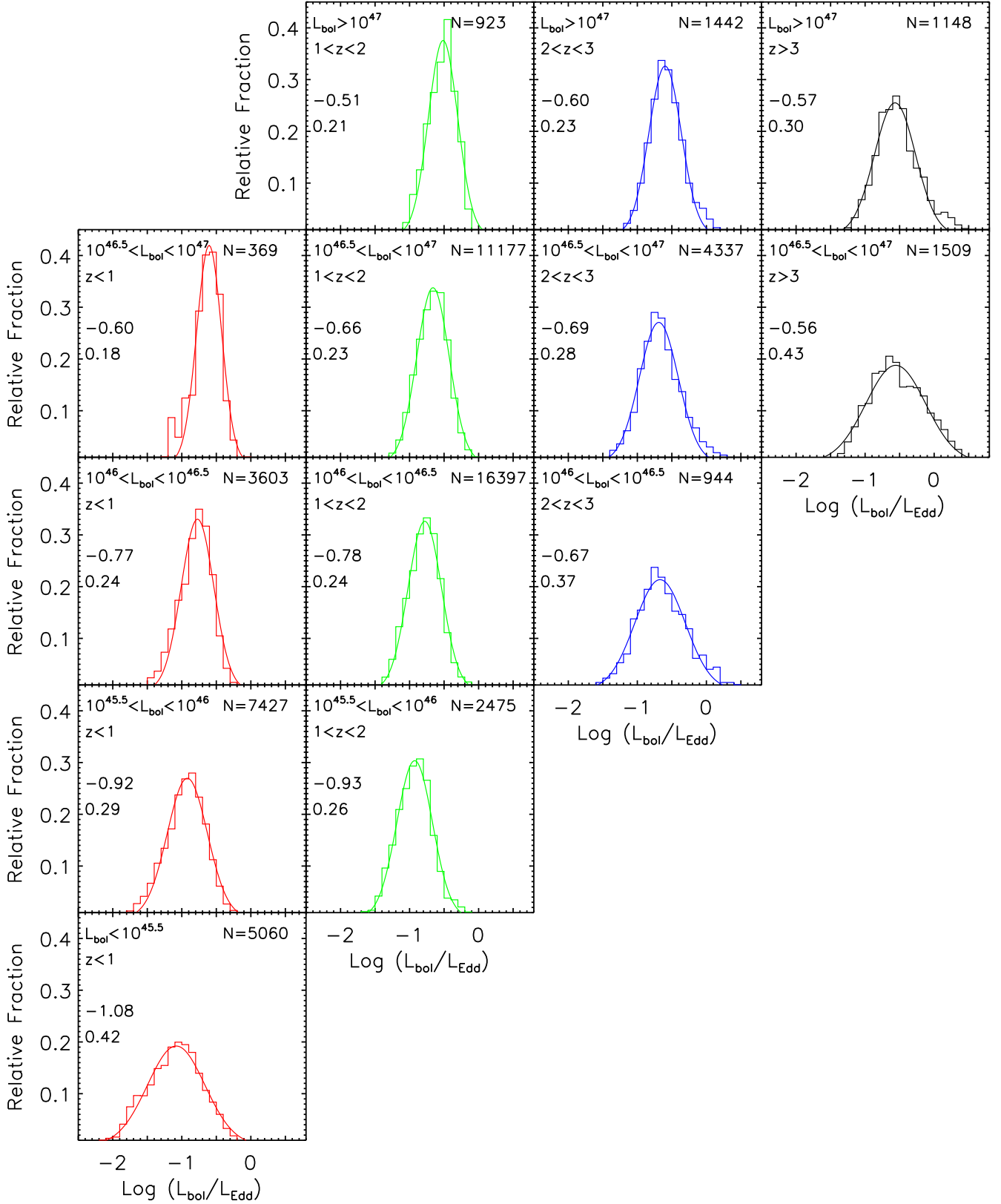


FIG. 12.— Apparent distributions of Eddington ratios $\log(L_{\text{bol}}/L_{\text{Edd}})$ based on virial BH masses in various redshift and luminosity bins. Also plotted are the fitted Gaussians, with the means and dispersions shown in the middle-left in each panel. The number of objects in each bin is shown in the upper-right corner.

TABLE 2
MODEL PARAMETERS

Redshift	γ_M	C_1	C_2	σ_E (dex)	σ_{FWHM} (dex)	σ_{vir} (dex)
$0.7 < z < 1.0$	-2.6	-3.60	0.3	0.4	0.11	0.33
$1.9 < z < 2.1$	-2.6	-2.88	0.2	0.4	0.11	0.31

NOTE. — See the text for symbol meanings.

The parameters C_1 , C_2 , and σ_{FWHM} are jointly constrained by the observed FWHM distribution in our sample: if the central Eddington ratio is too large or too small, the central value of FWHM will be correspondingly under(over)estimated; if the slope C_2 between $\log M_{\text{BH,true}}$ and $\langle \log L_{\text{bol}}/L_{\text{Edd}} \rangle$ is too small, the central FWHM will show a systematic trend with BH mass and luminosity stronger than the one we actually observe; if σ_{FWHM} is too large, then the observed FWHM distribution will be too broad. The comparison between the observed FWHM distribution and the simulated one must be made in each luminosity bin separately. Once we are able to reproduce the FWHM distribution and the luminosity distribution, we automatically reproduce the virial BH mass and apparent Eddington ratio distributions.

Finally, σ_E and σ_{FWHM} are jointly constrained by the requirement $\sigma_{\text{vir}} = \sqrt{(b\sigma_E)^2 + (2\sigma_{\text{FWHM}})^2} \gtrsim 0.3$ dex. If both σ_E and σ_{FWHM} are too small, we will predict an uncertainty of $\sigma_{\text{vir}} < 0.3$ dex, an accuracy below that of reverberation mapping. We will discuss this point further in §5.3.

4.4. Results

We carry out the comparison between our simulation for a given set of model parameters and the observed distributions at three luminosity bins in each redshift bin. We systematically and manually search the parameter space to find values where the simulated distributions agree with observations, judged by eye. The best-fit parameters are listed in Table 2. We have not searched the parameter space exhaustively enough to claim unequivocally that these solutions are unique, but the arguments we gave at the end of the previous section suggest it is unlikely that there is another region of parameter space which will satisfy all the constraints. Of course, more complicated models (e.g., deviations from a pure power law in the mass distribution) could also be found with different parameters. Note also that we do not quote formal errors on the parameters, given the way in which we found the best solution.

Given the sets of parameters in Table 2, eq. 4 yields an uncertainty of the virial masses at fixed true BH mass of $\sigma_{\text{vir}} = 0.33$ dex and 0.31 dex for the MgII and CIV cases respectively⁸. The central Eddington ratio for a typical quasar with $M_{\text{BH,true}} = 10^8 M_{\odot}$ is $\langle \log L_{\text{bol}}/L_{\text{Edd}} \rangle = -1.2$ and -1.3 for the two cases; the (insignificant) difference arises because of the difference in the virial relations and in the observed FWHM distributions. These distributions of Eddington ratios must be interpreted with care, since they are heavily dependent on the exact forms and scatter of the virial relations, which are not well-understood at this time.

The comparison of the simulated and observed results are displayed in three luminosity bins in Figs. 13 (for MgII)

⁸ These values are slightly smaller than the observed values (e.g., McLure & Jarvis 2002; Vestergaard & Peterson 2006), but our σ_{vir} is the scatter at fixed BH mass, while the quoted uncertainties are determined from a sample of reverberation mapping objects covering a range of BH masses.

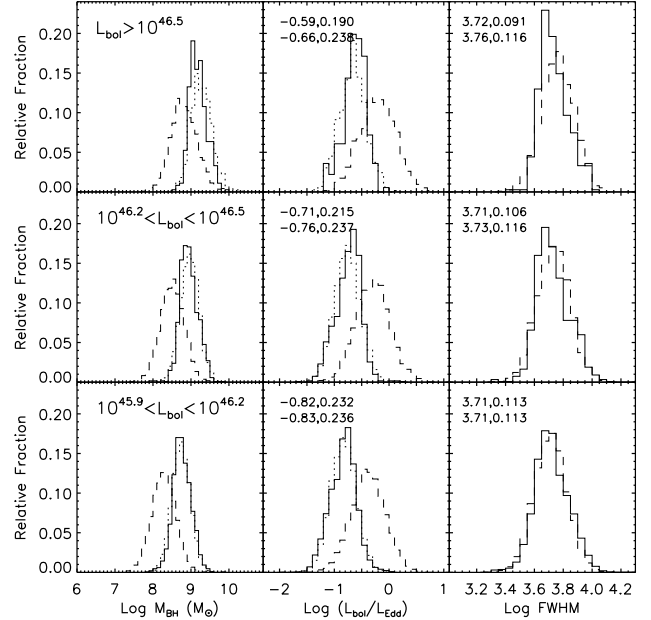


FIG. 13.— Comparison between observed and simulated distributions for MgII at $0.7 < z < 1.0$. The assumed underlying true BH mass distribution is a power-law with slope $\gamma_M = -2.6$. The assumed Eddington ratio distribution at fixed true BH mass is $\log L_{\text{bol}}/L_{\text{Edd}} = -3.6 + 0.3 \log M_{\text{BH,true}} + \sigma_E$, where $\sigma_E = 0.4$ dex. The survey is complete above $\log \left(\frac{L_{\text{bol}}}{\text{erg s}^{-1}} \right) = 45.9$, and the observed slope $\gamma_L \sim -2$ in the power-law distribution of bolometric luminosities is reproduced. Each comparison is done for three luminosity bins arranged in rows. In each panel, the solid histograms are observed distributions; the dotted histograms are simulated distributions for virial masses and apparent Eddington ratios based on virial masses. In the BH mass and Eddington ratio panels, we also show the distributions of the true underlying BH masses and Eddington ratios in dashed histograms. The simulated FWHM distributions in the third column are shown as dashed histograms. In the second and third column, the numbers show the mean and σ of the fitted log-normal for both the observed (upper) and simulated (lower) distributions.

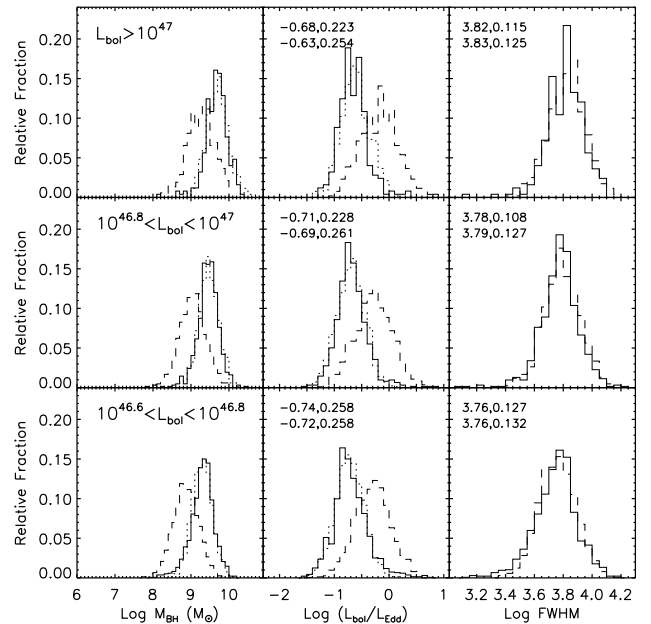


FIG. 14.— Comparison between observed and simulated distributions for CIV at $1.9 < z < 2.1$. The assumed underlying true BH mass distribution is a power-law with slope $\gamma_M = -2.6$. The assumed Eddington ratio distribution at fixed true BH mass is $\log L_{\text{bol}}/L_{\text{Edd}} = -2.88 + 0.2 \log M_{\text{BH,true}} + \sigma_E$ with $\sigma_E = 0.4$ dex. The survey is complete above $\log \left(\frac{L_{\text{bol}}}{\text{erg s}^{-1}} \right) = 46.6$, and the observed slope $\gamma_L \sim -2$ in the power-law distribution of bolometric luminosities is reproduced. Notations are similar to Fig. 13.

and 14 (for CIV). The figures show the distributions of BH masses (left), Eddington ratios (middle) and FWHMs (right). Our simulations are very successful at reproducing the observed distributions of virial BH masses, Eddington ratios and FWHMs. The virial BH masses (solid and dotted histograms) on average overestimate the true BH masses (dashed histograms) in each luminosity bin because of the Malmquist bias caused by the finite scatter of the black hole mass estimator (the part of scatter in virial masses that originates from luminosity) and the fact that there are more low-mass than high-mass black holes.

The widths of the observed BH mass and Eddington ratio distributions in each luminosity bin are smaller than those of the true quantities, and the Eddington ratios are biased low. However, although there are more quasars at the faint luminosity end, these faint objects are rarely scattered into high-luminosity bins, because of the finite width of the true Eddington ratio distribution. Running our model in alternate redshift bins ($1.5 < z < 1.7$ for MgII and $3.0 < z < 3.2$ for CIV) yields similar parameters. Thus our model is consistent with a non-evolving true Eddington ratio distribution, at least at the current levels of observations.

There are objects with $L_{\text{bol}}/L_{\text{Edd}} > 1$ in Figs. 13 and 14, caused by the high-luminosity tail in the scatter $\sigma_E = 0.4$ dex at individual BH masses. However, the fraction of these super-Eddington objects is small and the formal Eddington limit is only approximate. Enforcing a cutoff in the model Eddington ratio distribution has little effect on our conclusions.

Malmquist bias will be present independent of any luminosity cut on the sample, given the scatter between the true and “observed” masses and a bottom-heavy true BH mass distribution. This Malmquist-type bias is important in analyses that are based on “observed” BH masses, such as the active BH mass function (e.g., McLure & Dunlop 2004) and the redshift-evolution of the $M - \sigma$ relation (Lauer et al. 2007).

We have demonstrated the Malmquist bias with simulations, but the form of the bias can be shown analytically. We start by deriving the bias at fixed observed virial mass, and then generalize to the bias at fixed observed luminosity. Following Lynden-Bell et al. (1988), we model the probability distribution of $m_e \equiv \ln M_{\text{BH,vir}}$ given $m \equiv \ln M_{\text{BH,true}}$ as a Gaussian; that is:

$$p_0(m_e|m) = (2\pi\Delta_m^2)^{-1/2} \exp\left[-\frac{1}{2}(m-m_e)^2/\Delta_m^2\right], \quad (5)$$

where $\Delta_m = (\ln 10)\sigma_{\text{vir}}$ is the Gaussian σ . Let $nd \ln M_{\text{BH,true}}$ be the number of BHs with masses between $\ln M_{\text{BH,true}}$ and $\ln M_{\text{BH,true}} + d \ln M_{\text{BH,true}}$. For a power-law distribution of the underlying true BH masses, $n \propto M_{\text{BH,true}}^{\gamma_M}$, we have:

$$n \frac{dM_{\text{BH,true}}}{M_{\text{BH,true}}} \equiv n dm \propto M_{\text{BH,true}}^{\gamma_M-1} dM_{\text{BH,true}} \propto e^{\gamma_M m} dm, \quad (6)$$

where γ_M is our assumed slope in the underlying power-law BH mass distribution. Then the distribution of m for a given m_e is

$$\begin{aligned} p_1(m|m_e) &= p_0 e^{\gamma_M m} \left[\int p_0 e^{\gamma_M m} dm \right]^{-1} \\ &= (2\pi\Delta_m^2)^{-1/2} \exp\left\{-\frac{1}{2}[m-(m_e+\gamma_M\Delta_m^2)]^2/\Delta_m^2\right\}. \end{aligned} \quad (7)$$

This is a Gaussian distribution, centered on the mass $\langle m \rangle = m_e + \gamma_M \Delta_m^2$ and therefore the bias in log mass is

$-\gamma_M \Delta_m^2 / \ln 10$. Inserting $\gamma_M = -2.6$, $\sigma_{\text{vir}} \approx 0.3$ and $\Delta_m = (\ln 10)\sigma_{\text{vir}} \approx 0.7$ produces a bias in log mass of 0.55 dex.

However, the Malmquist bias we derived above is the bias at fixed virial mass, not the bias at fixed luminosity (Figs. 13 and 14). To calculate the latter, we proceed similarly.

Let $l \equiv \ln L_{\text{bol}}$ and $m \equiv \ln M_{\text{BH,true}}$, then the probability distribution of l at fixed m is:

$$p_0(l|m) = (2\pi\Delta_l^2)^{-1/2} \exp\left[-\frac{[l-(C_3+C_4m)]^2}{2\Delta_l^2}\right], \quad (8)$$

where the constants $C_3 \equiv [C_1 + \log(1.3 \times 10^{38})] \ln 10$, $C_4 \equiv 1 + C_2$ and $\Delta_l \equiv (\ln 10)\sigma_E$ following equation (2).

The probability distribution of m at fixed l is then

$$\begin{aligned} p_1(m|l) &= p_0 e^{\gamma_M m} \left[\int p_0 e^{\gamma_M m} dm \right]^{-1} \\ &= \left(2\pi \frac{\Delta_l^2}{C_4^2}\right)^{-1/2} \exp\left\{-\frac{C_4^2}{2\Delta_l^2} \left[m - \frac{C_4(l-C_3) + \gamma_M \Delta_l^2}{C_4}\right]^2\right\}, \end{aligned} \quad (9)$$

which is a Gaussian distribution with dispersion Δ_l/C_4 centered on $\langle m \rangle = (l - C_3)/C_4 + \gamma_M \Delta_l^2/C_4^2$. A similar analysis for the distribution of the “observed” BH mass $m_e \equiv \ln M_{\text{BH,vir}}$ at fixed luminosity gives a Gaussian distribution with mean $\langle m_e \rangle = (l - C_3)/C_4$ and dispersion $2\sigma_{\text{FWHM}} \ln 10$. The Malmquist bias, i.e., the difference in the two means is $-\gamma_M \Delta_l^2/(C_4^2 \ln 10) \approx 0.6$ dex when plugging in numbers. The distribution of log true masses at fixed luminosity has a width of $\Delta_l/(C_4 \ln 10) = 0.32$ dex; while the distribution of log virial masses at fixed luminosity has a width of $\sigma'_{\text{vir}} = 2\sigma_{\text{FWHM}} = 0.22$ dex. These results are in excellent agreement with what we see in Figs. 13 and 14.

The Malmquist bias is mainly caused by the bottom-heavy true BH mass distribution and the scatter σ_{vir} in the virial estimators (or the uncorrelated scatter σ_E in the case of fixed luminosity). However, we emphasize that the exact magnitude and form of the bias depends in detail on the partition and behavior of the scatter in the virial relations. We have used $\sigma_E = 0.4$ dex and $\sigma_{\text{FWHM}} = 0.11$ dex in order to reproduce the observed uncertainty in virial BH estimators of $\sigma_{\text{vir}} \gtrsim 0.3$ dex and the observed FWHM distributions, but a smaller scatter of virial BH mass at fixed true mass would reduce the Malmquist bias. Also, the values of σ_E and σ_{FWHM} could depend on luminosity. Our data do not allow us to consider such refinements in detail. Since the Malmquist bias is proportional to γ_M , we expect a smaller bias for objects fainter than the break in the luminosity function, such as those in the AGES sample (Kollmeier et al. 2006).

Although our model of the underlying true BH mass and Eddington ratio distributions can roughly reproduce the observations, we have made a few simplifications. In particular, the largest uncertainty arises from the assumed virial relations and their scatters, for which there is no consensus yet. Changes in these virial relations (e.g., a different slope in the $R-L$ relation, etc., see Bentz et al. 2006; Netzer et al. 2007) will certainly change the values of our model parameters. We also note that there might be other systematic errors associated with virial BH masses or reverberation mapping masses in general (Krolik 2001). Given all the limitations and simplifications of our model, we do not wish to overinterpret our modeled distributions at this time, but rather highlight the danger that the virial masses for a population of quasars could be subject to serious systematic biases. Until we have both

TABLE 3
QUASAR BLACK HOLE MASS FUNCTION

z	$\Phi_{L_{\text{bol}} > 10^{46} \text{ erg s}^{-1}} \text{ (Mpc}^{-3}\text{)}$	$\Phi_{M_{\text{BH}} > 10^{9.5} M_{\odot}} \text{ (Mpc}^{-3}\text{)}$
0.85	2.87×10^{-6}	1.0×10^{-8}
2.0	1.20×10^{-5}	7.4×10^{-8}
3.1	8.08×10^{-6}	5.0×10^{-8}

better observations and a theoretical understanding of the systematic behavior of the virial estimators with BH properties, we urge caution in the interpretation of BH mass functions based on virial estimators.

4.5. Active BH mass function in quasars

Our model explicitly provides the true BH mass distribution and connects it to the bolometric luminosity distribution via our modelled Eddington ratio distribution, and thus provides an estimate of the underlying BH mass function in quasars based on our knowledge of the bolometric luminosity function.

An alternative method using optically selected samples uses the observed luminosity function and the fraction of BHs above a certain mass threshold within some luminosity range, to place lower limits on the number density of active BHs above the mass threshold (McLure & Dunlop 2004). The measurement is a lower limit simply because it neglects BHs scattered out of the luminosity range being considered. Using this method, McLure & Dunlop (2004) found that the majority of $> 10^{8.5} M_{\odot}$ SMBHs are already in place at $z \sim 2$ when geometric obscuration and quasar duty cycles were taken into account. However, their results were based on virial BH masses, and they did not take into account the Malmquist bias that we have discussed here.

Here we use our model to estimate the cumulative BH mass function in quasars above a certain mass threshold. Notice that the break in the bolometric luminosity function (Hopkins et al. 2007) is at $\log\left(\frac{L_{\text{bol}}}{\text{erg s}^{-1}}\right) \sim 46$ at $z \sim 1-3$, corresponding to $\log M_{\text{BH, true}} \sim 8.8-9.0$ in our model (e.g., equation 2). Thus our single power-law distribution of the underlying BH masses is inaccurate below this mass threshold⁹, and will affect the mapping from the BH mass function to the bolometric luminosity function. We will explore the effects of a break in a future paper.

We focus on the cumulative mass function above $10^{9.5} M_{\odot}$, i.e., the most massive SMBHs. The estimation is simple: we take our simulated catalogs at different redshifts and count the number of BHs with mass greater than $10^{9.5} M_{\odot}$ and the number of BHs with $\log\left(\frac{L_{\text{bol}}}{\text{erg s}^{-1}}\right) > 46$; the latter number is compared to the cumulative bolometric luminosity function (Hopkins et al. 2007, the “full” model in their table 3) with $\log L_{\text{bol}} > 46$ and normalized; then we use this normalization to estimate the number density of active BHs with $\log M_{\text{BH, true}} > 9.5$. Our results are listed in Table 3, for three redshift bins: $z = 0.7-1.0$, $1.9-2.1$, $3.0-3.2$. The number density of BHs with mass $> 10^{9.5} M_{\odot}$ in optical quasars peaks around $z \sim 2$, and then decreases at lower redshift.

The numbers above are lower limits on the total (active and inactive) SMBH population because of quasar duty cycles and the presence of obscured populations of active BHs

⁹ Our conclusions on the distributions of FWHMs and virial BH masses are insensitive to this detail. However, the Malmquist bias will be smaller below the break, as mentioned above.

at high redshift. Surveys in other wave bands, especially in the X-ray and infrared, are starting to reveal those missing active SMBHs (e.g., Treister et al. 2006; see also Zakamska et al. 2003), and will provide better constraints of the BH mass function at high redshift, given our knowledge of the local dormant BH mass function (e.g., Marconi et al. 2004; Merloni 2004). We note that the numbers derived here are fully consistent with current constraints on the local BH mass function at the high-mass end (e.g., Tundo et al. 2007; Lauer et al. 2007), and allow an additional boost factor of $\sim 10-20$ due to quasar duty cycles and geometric obscuration at $z \sim 2$.

4.6. Results for radio loud quasars and BALs

In this section, we determine virial BH masses for radio-loud quasars and BALs, to explore whether their black hole properties are distinctive from “ordinary” quasars of similar luminosity and redshift. The Eddington ratio and BH mass distributions will be affected by Malmquist bias, but the bias should be similar for each individual subsample, allowing this kind of comparison to be made.

For the radio analysis, we carve out a narrow range in redshift-luminosity space, $\log\left(\frac{L_{\text{bol}}}{\text{erg s}^{-1}}\right) = 46.6-46.75$ and $z = 1.5-2.3$, over which we have MgII virial masses for each source, and the *FIRST*-detected and undetected quasars have similar redshift and optical luminosity distributions. At these redshifts, the *FIRST* radio flux limit corresponds to a radio luminosity density of $\sim 3 \times 10^{25}$ Watts/Hz, which is radio-loud by all standard definitions. This region contains 3360 radio-undetected quasars and 170 radio-loud quasars. The radio-loudness, defined as $\mathcal{R} = f_{6 \text{ cm}}/f_{2500}$ for these *FIRST*-detected objects ranges from ~ 5 to ~ 4600 with median value ~ 100 , based on a subset of DR3 quasars studied by Jiang et al. (2007b). Fig. 15 shows that the MgII based virial mass distributions for the radio-undetected and radio-loud quasars are slightly different, with radio-loud quasars having slightly larger median value by ~ 0.12 dex, comparable to the results in McLure & Jarvis (2004). Radio-loud quasars in our sample have smaller Eddington ratios than radio-undetected quasars on average, as has been found in previous analyses (e.g., Ho 2002).

For BALs (most of which are CIV BALs), the situation is more complicated. First, BALs in general are more reddened than nonBALs (e.g., Reichard et al. 2003), affecting the bolometric luminosity estimates. Second, the broad absorption troughs can severely impact the reliability of FWHM measurements; the concerns about disk winds affecting the measurement of the CIV line (discussed in § 3.3.2) are especially important for BALs.

Fortunately, for $1.7 \lesssim z \lesssim 2.2$ we have both MgII and CIV, thus it becomes feasible to compare the difference in virial mass for high-ionization BALs (which appear in the CIV line only) and nonBALs, based on the MgII estimator. For the uniformly-selected quasar sample the redshift and luminosity distributions are almost identical for CIV BALs and nonBALs at $1.7 \lesssim z \lesssim 2.2$ (Shen et al. 2008). We choose uniformly-selected quasars that have redshift $1.7 \leq z \leq 2.2$ and have MgII based virial masses; the sample includes 5408 nonBALs and 796 BALs. Fig. 16 shows that their MgII virial mass distributions are quite similar, with median mass $\log M_{\text{BH, vir}} = 9.34$ for both. This result is consistent with recent findings by Ganguly et al. (2007) based on 5088 quasars from SDSS DR2, although the mean virial BH masses are different due to difference in the calibrations used and line measurements,

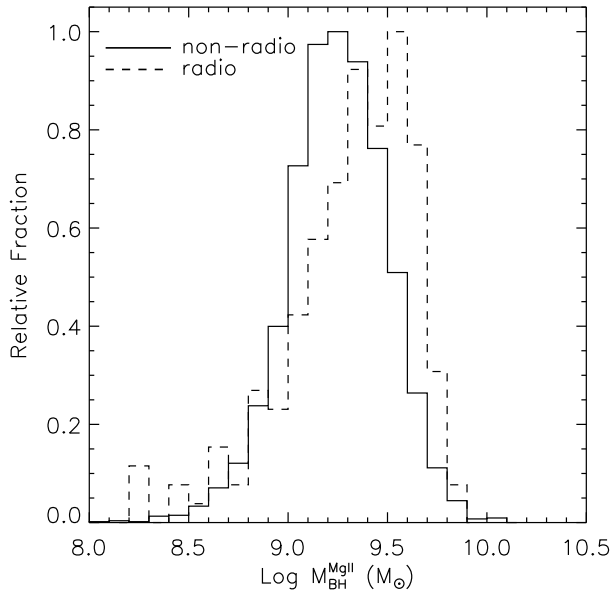


FIG. 15.— Distributions of MgII based virial masses for the radio-undetected (solid histogram) and radio-loud (dashed histogram) quasars in subsamples matched in redshift and luminosity distributions; see text.

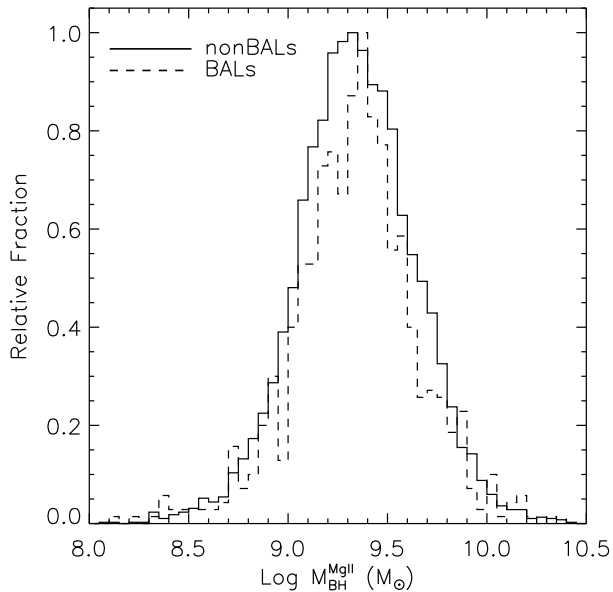


FIG. 16.— Distributions of MgII based virial masses for nonBALs (solid histogram) and BALs (dashed histogram) with $1.7 \leq z \leq 2.2$, which are within the uniformly-selected quasar sample. The redshift and luminosity distributions of nonBALs and BALs are identical.

as we discuss below. This similarity in virial BH masses for BALs and nonBALs supports the idea that BALs are intrinsically no different from nonBALs, and the BAL phenomenon is caused by different viewing angles with respect to a disk wind (e.g., Weymann et al. 1991; Elvis 2000). This picture is also consistent with our recent findings that BALs show similar large-scale clustering to nonBALs (Shen et al. 2008).

5. DISCUSSION

5.1. General issues with virial estimators

The virial BH mass measurements presented in this paper are consistent with, but not identical to results from a variety of papers (e.g., McLure & Dunlop 2004; Dietrich & Hamann

2004; Kollmeier et al. 2006; Ganguly et al. 2007). The difference in the mean of the distribution can be due to a variety of effects: different samples, different virial estimators and different calibrations for the same estimator, as well as different procedures to measure luminosities and line widths used in these virial estimators. We elaborate below how these various choices lead to differences in virial masses even for a given underlying sample.

5.1.1. Different virial calibrations for the same line estimator.

There are several versions in the literature of a given virial estimator, and they do not generally yield the same virial mass when applied to SDSS or other quasar/AGN samples. For example, the $H\beta$ calibrations in McLure & Dunlop (2004) and in Vestergaard & Peterson (2006) differ by ~ 0.17 dex given the mean luminosity $\lambda L_{\lambda,5100} \sim 10^{44.6}$ erg s^{-1} in our sample. Likewise, for the MgII estimator, the version in McLure & Dunlop (2004) yields a larger virial mass by ~ 0.3 dex for $\lambda L_{\lambda,3000} = 10^{46.1}$ erg s^{-1} (which corresponds to SDSS quasars at $z \sim 2$), than the older version in McLure & Jarvis (2002). The latter case partially explains the discrepancy between our measurements and a subset of our sample measured by Ganguly et al. (2007). While we have used the most recent calibrations available (McLure & Dunlop 2004; Vestergaard & Peterson 2006), it is quite likely that those calibrations will change when the updated $R-L$ relation and virial coefficient (zero-point offset) are incorporated (Onken et al. 2004; Bentz et al. 2006; Kaspi et al. 2007).

5.1.2. Different ways to measure luminosity and FWHM.

Even for the same calibration, different authors have used a variety of ways to measure luminosity and line width parameters, which will lead to systematically different results. For example, the mean MgII FWHM taken from the broad component of a two-Gaussian fit is larger by ~ 0.15 dex than the non-parametric FWHM measured from the modelled spectrum which best reproduces the line profile. This contributes to the underestimation of the MgII based virial masses (e.g., Dietrich & Hamann 2004; Ganguly et al. 2007). For CIV, on the other hand, it is more reasonable to use the FWHM measured from the modelled flux that best reproduces the CIV line profile because that is how the CIV relation is calibrated (e.g., Vestergaard & Peterson 2006). Although some argue that a narrow-line component is present in the CIV line (e.g., Marziani et al. 1996) and recipes have been provided for subtracting it (cf., Bachev et al. 2004), we cannot perform such an exercise until the CIV estimator is re-calibrated with narrow-line-subtracted line widths. Indeed, it is *crucial* to use the methods of measuring FWHMs used in the original calibrations of these virial relations if one wants to obtain unbiased results. We feel confident about our choices, as we found no mean offset between virial masses based on different lines (Figs. 5 and 9).

5.1.3. Other issues with our measurements.

There are some additional factors that might lead to differences between our measurement and others for the same sample of quasars. First, the spectroscopic flux scale used in this study is higher than previous SDSS data releases (DR5 and prior) by ~ 0.14 dex, giving rise to a systematic ~ 0.07 dex increase in virial masses. Second, we have separated the broad and narrow components of $H\beta$ and MgII at a FWHM of 1200 km s^{-1} , following Hao et al. (2005). It is possible that

we are biasing the mean virial mass by doing so. Nevertheless, these effects are minor considering the uncertainties in the zero-point offsets of these virial estimators.

As we discussed in §4.2, given the independence of the observed FWHM distribution with luminosity, objects in the $M_{\text{BH,vir}} - L_{\text{bol}}$ plane tend to lie on a narrow stripe with a slope $b \sim 0.5$ (see Fig. 11). The lower-luminosity high redshift quasars in the Kollmeier et al. (2006) sample would also fall on the stripe. The mean apparent Eddington ratio $(\log(L_{\text{bol}}/L_{\text{Edd}}))_{\text{vir}} \propto (1-b)\log L_{\text{bol}}$. Thus the expected $\langle \log(L_{\text{bol}}/L_{\text{Edd}}) \rangle_{\text{vir}}$ would be ~ -1.75 for $\log\left(\frac{L_{\text{bol}}}{\text{erg s}^{-1}}\right) = 44$, ~ -2.25 for $\log\left(\frac{L_{\text{bol}}}{\text{erg s}^{-1}}\right) = 43$, and ~ -3.25 for $\log\left(\frac{L_{\text{bol}}}{\text{erg s}^{-1}}\right) = 41$ for $b \sim 0.5$. These Eddington ratio values are in good agreement with the typical Eddington ratios from X-ray selected AGN samples which cover the bolometric luminosity range $L_{\text{bol}} \sim 10^{41} - 10^{44} \text{ erg s}^{-1}$ (e.g., Panessa et al. 2006; Babić et al. 2007; Ballo et al. 2007). However, there are two reasons to be cautious about this apparent agreement: current X-ray selected AGN samples still suffer from limited sample size and various incompletenesses, and most of the BH masses in X-ray selected AGN are estimated based on host galaxy properties rather than virial methods, and it remains unclear how good these methods agree with each other for those low-luminosity BHs.

On the other hand, virial methods have their own limitations due to their reliance on poorly understood BLR physics. If the existence of the broad line region itself depends on Eddington ratio, then it is not surprising that broad line AGN/quasars lie preferentially within a favorable Eddington ratio range. Moreover, the width of the Eddington ratio distribution at fixed luminosity could be underestimated, if, for example, the line widths only partially reflect the virial velocities in the BLR, as we will further discuss in §5.3.

5.2. Limitations of the SDSS sample

Although the large size of the SDSS sample provides unprecedented statistics, we feel obligated to point out its limitations.

First, the dynamic range in luminosity is narrow for SDSS quasars. Only luminous quasars are included in the flux-limited sample. Other surveys, such as the AGES survey (Kochanek et al. 2004) and the 2dF-SDSS LRG and QSO (2SLAQ) Survey (Cannon et al. 2006) extend to fainter luminosities at the same redshift. Our sample does include some objects of lower luminosity, but they are incomplete in ways that are hard to quantify.

Second, the wavelength range of SDSS spectra has forced us to use different virial estimators at different redshift. Although we cross-compared virial relations of $\text{H}\beta$ - MgII and MgII - CIV , the direct comparison between the $\text{H}\beta$ and CIV estimators is impossible with SDSS spectra. Thus it is important to study these broad lines simultaneously with multi-band spectra (e.g., Sulentic et al. 2000 and references therein; Baskin & Laor 2005). It is also desirable to obtain near-IR spectra for high-redshift quasars with optical spectra, to get $\text{H}\beta$ or MgII measurements (e.g., Sulentic et al. 2006; Jiang et al. 2007a; Kurk et al. 2007; Netzer et al. 2007), since the CIV virial estimator alone is perhaps questionable for the reasons we have discussed in this paper.

5.3. Issues with our model

In §4.3 we introduced a statistical model which can reproduce the observed luminosity and FWHM distributions. We now provide some justifications of our choices of model parameters, and discuss the connections between the real physical quantities, i.e., BLR size and virial velocity, and their surrogates, luminosity and FWHM.

An important assumption of our model is the origin of the uncertainties in virial estimators, i.e., for fixed true BH mass, the virial estimator will give an estimate log-normally distributed around the right mean value and with dispersion σ_{vir} . However, the value of σ_{vir} remains unclear: the rms scatter of virial masses around reverberation mapping (RM) masses (e.g., McLure & Jarvis 2002; Vestergaard & Peterson 2006) is 0.3–0.4 dex, comparable to the rms scatter of virial masses around BH masses derived from the $M - \sigma$ relation (e.g., Greene & Ho 2006); but the relationship of this number to the scatter around *fixed true* BH mass is unknown. Given all the issues with virial estimators we discussed in §5.1, it seems unlikely that virial estimates based on single-epoch spectra are good to a factor of 2, an accuracy that can barely be achieved with reverberation mapping. Therefore we believe our choice of $\sigma_{\text{vir}} \gtrsim 0.3$ dex is appropriate.

At a given true BH mass, in our simplistic model, the broadening of the luminosity distribution is completely uncorrelated with the broadening of the FWHM distribution. Are our required values for the uncorrelated scatters σ_{E} and σ_{FWHM} consistent with observations? Current reverberation mapping data indicate a scatter of $\sim 0.2 - 0.35$ dex in luminosity at fixed BLR size (e.g., Kaspi et al. 2005; Bentz et al. 2006). The best studied reverberation mapping sources indicate scatters of ~ 0.1 dex in line width at fixed BLR size for a given object (e.g., Bentz et al. 2007). These values are for a handful of well studied objects with reverberation mapping of the $\text{H}\beta$ line only, and we might expect somewhat larger scatters for both luminosity and line width in samples with a wider range of luminosity and redshift than probed by current RM samples. Thus while our choices of uncorrelated scatters $\sigma_{\text{E}} = 0.4$ dex and $\sigma_{\text{FWHM}} = 0.11$ dex may appear rather large, they are at least plausible.

We still expect some component of the variations in luminosity to correlate directly with variations in FWHM, as is seen in local samples. Here we investigate what magnitude of correlated broadening can be supported given existing observations. At fixed true BH mass, the virial mass estimate is expressed in terms of its luminosity and FWHM:

$$\begin{aligned} \log M_{\text{BH,vir}} &= C + b \log L_{\text{bol}} + 2 \log \text{FWHM} \\ &= C + b \left(\langle \log L_{\text{bol}} \rangle + \delta_{\text{E}} + \delta_{\text{corr}} \right) \\ &\quad + 2 \left(\langle \log \text{FWHM} \rangle + \delta_{\text{FWHM}} - 0.5b\delta_{\text{corr}} \right), \end{aligned} \quad (10)$$

where b is the slope of the $R - L$ relation, the various δ_i denote Gaussian-random variables with dispersions σ_i , and other constants have been absorbed in C . At this fixed true BH mass, the bolometric luminosity and the FWHM both follow a log-normal distribution, $\log L_{\text{bol}} = \langle \log L_{\text{bol}} \rangle + \delta_{\text{E}} + \delta_{\text{corr}}$ and $\log \text{FWHM} = \langle \log \text{FWHM} \rangle + \delta_{\text{FWHM}} - 0.5b\delta_{\text{corr}}$. In addition to the uncorrelated terms δ_{E} and δ_{FWHM} as modelled in §4.3, we also introduced correlated variations δ_{corr} and $-0.5b\delta_{\text{corr}}$ in luminosity and FWHM, respectively, whose amplitude we will constrain below. Note that these correlated terms cancel each other out, and hence do not contribute to the uncertainty in the virial relation.

The correlated terms in equation (10) reflect the intrinsic variation in BLR size/virial velocity at fixed true BH mass.

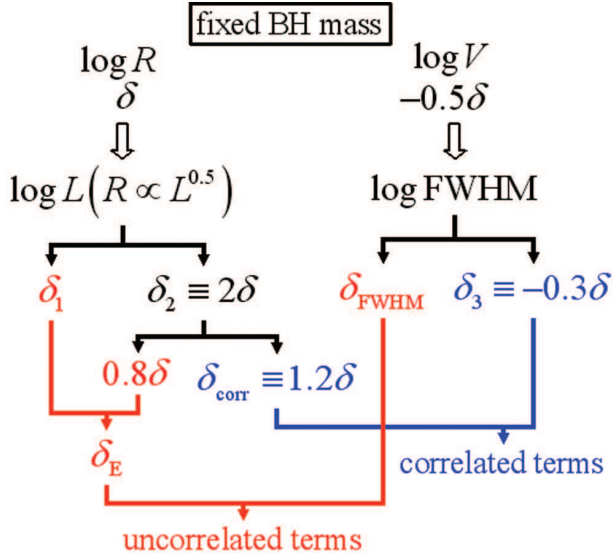


FIG. 17.— Schematic plot showing the relations between the actual physical quantities, i.e., BLR radius $\log R$ and virial velocity $\log V$ that determine the BH mass, and their surrogates, luminosity $\log L$ and line width $\log \text{FWHM}$. The mean $R-L$ relation is assumed to have a slope 0.5. The mean relation between $\log \text{FWHM}$ and $\log R$ is assumed to have a slope -0.3 in this particular example, i.e., not a perfect virial relation with slope -0.5 . The intrinsic variations of BLR radius and virial velocity are δ and -0.5δ at this fixed true BH mass. For luminosity, δ_1 is the rms scatter around the $R-L$ relation and $\delta_2 \equiv 2\delta$ is the variation that drives the variation in BLR size. For FWHM, δ_{FWHM} is the rms scatter around the mean FWHM-virial velocity relation, and $\delta_3 \equiv -0.3\delta$ is the part that responds to the variations in BLR size. Terms in red end up to be the *uncorrelated* variations δ_E and δ_{FWHM} in our model, which contribute to the uncertainty of the virial estimator. Terms in blue end up to be the *correlated* variations that do not contribute to the virial uncertainty.

In our model formalism in §4.3 we have set $\sigma_{\text{corr}} = 0$. Since our observed FWHM distributions are quite narrow, we found that we need¹⁰ $\sigma_{\text{corr}} \lesssim 0.2$ dex, such that the distribution of simulated FWHMs will not be broader than the observed distribution, keeping the requirement that $\sigma_{\text{vir}} \gtrsim 0.3$ dex. With this limit, the intrinsic dispersion in BLR size for our sample is $\sigma_{\text{BLR}} \lesssim 0.1$ dex at fixed true BH mass, which is narrower than the typical dispersion in BLR size inferred from less luminous reverberation mapping sources. It is possible that the intrinsic dispersion of BLR size at fixed true BH mass is indeed smaller for higher-luminosity objects. Reverberation mapping data for high luminosity objects are required to test this scenario.

One could also get a small apparent dispersion in BLR size if systematics in the BLR virial velocity-line width relation cause the FWHM to only partially trace real variations in the virial velocity. In other words, the *mean* relation in the $\log \text{FWHM} - \log R$ diagram for fixed BH mass could have a slope shallower than -0.5 , as has been suggested by Bentz et al. (2007) in $H\beta$ reverberation studies in NGC 5548. A non-virial-gas contaminated line width and/or inappropriate methods to measure line width could lead to this problem. The effects of this are illustrated in a specific worked example in Fig. 17, which shows how the intrinsic variations in the true BLR size (δ) and in the true virial velocity (-0.5δ , exactly compensating) for a given true BH mass might be parcelled out. The dispersion of observed luminosity is composed of

the portion that fully reflects the intrinsic variation in BLR size $\delta_2 \equiv 2\delta$ (where $b = 0.5$ is assumed), and the portion of rms scatter around the mean $R-L$ relation δ_1 . The dispersion of FWHM is composed of the portion that only partly reflects the intrinsic variation in virial velocity -0.3δ (i.e., a slope of -0.3 is assumed for the *mean* $\log R - \log \text{FWHM}$ relation in this particular example), and the portion of rms scatter around the *mean* virial velocity-FWHM relation, δ_{FWHM} . Dividing δ_2 into two terms: the $\delta_{\text{corr}} \equiv 1.2\delta$ term cancels with the -0.3δ variation in FWHM, i.e., these are the correlated terms defined earlier; the remaining 0.8δ portion in δ_2 combines with δ_1 to form δ_E . Hence, in this case, although δ_E is the uncorrelated term in luminosity according to our original definition, it still includes a portion that reflects the intrinsic variation in BLR size, and it contributes to the uncertainty in virial estimators. The intrinsic variation in BLR size can now be slightly broader, i.e., $\sigma_{\text{BLR}} \lesssim 0.17$ dex.

6. CONCLUSIONS

We have measured virial BH masses for 58,664 quasars in the SDSS DR5 quasar catalog. We used and compared three virial estimators: $H\beta$ ($z < 0.7$), MgII ($0.7 < z < 1.9$) and CIV ($z > 1.9$). We emphasized the importance of using the original definitions of line width and luminosity in whichever virial calibration is used. Our main conclusions are the following:

1. Within our sample, the line widths follow a log-normal distribution; their means and dispersions depend only weakly on redshift and luminosity.
2. For a subsample of quasars for which both the $H\beta$ and the MgII estimators are available, the ratio of their FWHMs follows a log-normal distribution with mean 0.0062 and a dispersion of 0.11 dex; the ratio of virial BH masses based on the two lines also follows a log-normal with mean 0.034 and a dispersion of 0.22 dex. Therefore, the MgII and $H\beta$ estimators give consistent results.
3. We further compared the MgII and CIV estimators in a subsample of quasars with both lines. Their FWHM ratio follows a log-normal with mean 0.027 dex and dispersion 0.18 dex; the ratio of their virial estimates follows a log-normal with mean -0.06 dex and dispersion 0.34 dex. Thus virial BH estimates are consistent using both lines, although with larger scatter than between $H\beta$ and MgII . However, the dispersion in the FWHM ratios is comparable to or even larger than the dispersion of the MgII and CIV FWHM distributions themselves, and the MgII FWHM and CIV FWHM are weakly correlated at best (see Fig. 8). Furthermore, the CIV estimator tends to give smaller virial masses than the MgII estimator for objects with small blueshifts ($\lesssim 1000 \text{ km s}^{-1}$), and conversely for objects with larger blueshifts. The reason for this systematic bias is attributed to the geometry of the BLR. The CIV line shows many features that suggest a component from non-virialized gas such as a disk wind (Murray et al. 1995; Proga et al. 2000; Elvis 2000). Therefore the CIV FWHM is perhaps not a good indicator of the BLR virial velocity. The current calibration of the CIV estimator gives consistent results with those using the other two estimators in the mean, but we caution that the bias may be large for individual objects.

¹⁰ This upper limit is set by the condition that the width of the correlated part $-0.5b\delta_{\text{corr}}$ is half of σ_{FWHM} in FWHM so that its contribution to the broadening of the FWHM distribution is negligible when added in quadrature.

4. The typical range of virial BH masses in the SDSS quasar sample is $10^8 - 10^{10} M_{\odot}$. The upper envelope of the virial mass distribution rises up to $z \sim 2$ and then flattens out. There is a clear upper limit $\sim 10^{10} M_{\odot}$ for all quasars, as other studies have found (e.g., McLure & Dunlop 2004; Vestergaard 2004).
5. Quasars lie in a narrow stripe in the mass and luminosity diagram (Fig. 11) bounded by $L_{\text{bol}} = 0.01L_{\text{Edd}}$ and $L_{\text{bol}} = L_{\text{Edd}}$, consistent with recent findings (e.g., Woo & Urry 2002; Kollmeier et al. 2006). However, this distribution is implicitly constrained by the virial relations and the observed FWHM distributions. Similar to the findings of Kollmeier et al. (2006), the distributions of apparent Eddington ratios $L_{\text{bol}}/L_{\text{Edd}}$ based on virial BH masses in different redshift-luminosity bins follow log-normal distributions, with means between $L_{\text{bol}}/L_{\text{Edd}} \approx 10^{-1.1}$ and $10^{-0.6}$. The widths of these distributions are typically ~ 0.3 dex or less.
6. The narrowness in the observed Eddington ratio (and virial mass) distributions within each luminosity bin is interpreted as arising from the combination of luminosity cuts and the underlying distributions of FWHMs; it is not the same as the intrinsic uncertainty in the virial mass estimators. By assuming an underlying true BH mass distribution and an Eddington ratio distribution at fixed true BH mass, together with the assumptions that the observed luminosity and FWHM are imperfect tracers of the virial BH mass, we were able to reproduce the observed distributions of luminosities, FWHMs, virial BH masses and apparent Eddington ratios in each luminosity bin. Monte Carlo simulations demonstrate that the observed virial BH mass and apparent Eddington ratio distributions are subject to Malmquist bias, i.e., more lower-mass BHs are scattered upwards due to the scatter between virial mass and true BH mass than higher-mass BHs are scattered down. To better quantify this Malmquist bias we need a better understanding of the form and scatter in the virial relations.
7. We also compared the distributions of virial BH masses for radio-loud quasars and BALs with that of “ordinary” quasars matched in redshift and luminosity. The mean virial mass of radio quasars is ~ 0.12 dex larger than that of ordinary quasars, but the mass distribution of BALs is indistinguishable from that of ordinary quasars.

With ever larger quasar samples, it has now become feasible to measure the clustering properties of quasars, and to directly test galaxy formation scenarios within the hierarchical structure formation framework (e.g., Shen et al. 2007 and reference therein). The clustering measured in current quasar samples shows only a weak luminosity dependence at $z \lesssim 2.5$ (e.g., da Ângela et al. 2007). Since BH mass is tightly correlated with bulge properties (e.g., Tremaine et al. 2002), we expect a correlation between BH mass and host dark matter halo mass (e.g., Ferrarese 2002). The fact that luminosity does not strongly correlate with clustering strength seems to indicate that the instantaneous quasar luminosity is not a good indicator of BH mass (Lidz et al. 2006). In fact, both in our model and in the data itself we see a significant range in luminosities at a fixed BH mass (see Figs. 13 and 14). We plan to

study quasar clustering as a function of virial BH mass, taking care to incorporate the effects of the uncertainties in the virial estimators and the Malmquist bias.

Despite the biases we have identified in this paper, the virial estimators are irreplaceable tools for estimating BH masses in AGN/quasars. One must simply be very careful when interpreting these virial masses for individual objects and for statistical samples. We point out that our methodology here can be applied to future data sets which push to lower luminosity AGN/quasars at all redshifts. It will be particularly interesting to probe below the break in the quasar luminosity function, where the Malmquist bias should be smaller and where it has been suggested that the Eddington ratio should be smaller as well (e.g., Hopkins et al. 2006). This will allow us to explore both the low-mass end of the BH mass function, and to study the nature of objects with low Eddington ratio at high redshifts. In addition, there is a strong need for better understanding of the forms and scatter in the virial relations.

We thank the anonymous referee for helpful comments, Marianne Vestergaard for advice on the usage of the CIV estimator and providing a UV iron template and Todd Boroson for the optical iron template. We acknowledge Daniel Proga for helpful discussions on BLR geometry, and Linhua Jiang for providing his radio-loudness measurements for SDSS quasars. We also want to thank Juna Kollmeier, Scott Tremaine, and especially David Weinberg for reading the manuscript and providing various suggestions that have greatly improved the draft. YS and MAS acknowledge the support of NSF grants AST-0307409 and AST-0707266. Support for JEG was provided by NASA through Hubble Fellowship grant HF-01196 awarded by the Space Telescope Science Institute, which is operated by the Association of Universities for Research in Astronomy, Inc., for NASA, under contract NAS 5-26555. DPS acknowledges the support of NSF grant AST-0607634.

Funding for the SDSS and SDSS-II has been provided by the Alfred P. Sloan Foundation, the Participating Institutions, the National Science Foundation, the U.S. Department of Energy, the National Aeronautics and Space Administration, the Japanese Monbukagakusho, the Max Planck Society, and the Higher Education Funding Council for England. The SDSS Web Site is <http://www.sdss.org/>.

The SDSS is managed by the Astrophysical Research Consortium for the Participating Institutions. The Participating Institutions are the American Museum of Natural History, Astrophysical Institute Potsdam, University of Basel, University of Cambridge, Case Western Reserve University, University of Chicago, Drexel University, Fermilab, the Institute for Advanced Study, the Japan Participation Group, Johns Hopkins University, the Joint Institute for Nuclear Astrophysics, the Kavli Institute for Particle Astrophysics and Cosmology, the Korean Scientist Group, the Chinese Academy of Sciences (LAMOST), Los Alamos National Laboratory, the Max-Planck-Institute for Astronomy (MPIA), the Max-Planck-Institute for Astrophysics (MPA), New Mexico State University, Ohio State University, University of Pittsburgh, University of Portsmouth, Princeton University, the United States Naval Observatory, and the University of Washington.

Facilities: Sloan

REFERENCES

- Abazajian, K., et al. 2005, *AJ*, 129, 1755 (DR3)
- Adelman-McCarthy, J. K., et al. 2007a, *ApJS*, 172, 634 (DR5)
- Adelman-McCarthy, J. K., et al. 2007b, *ApJS*, in press (DR6; arXiv:0707.3413)
- Babić, A., Miller, L., Jarvis, M. J., Turner, T. J., Alexander, D. M., & Croom, S. M. 2007, *A&A*, 474, 755
- Bachev, R., Marziani, P., Sulentic, J. W., Zamanov, R., Calvani, M., & Dultzin-Hacyan, D. 2004, *ApJ*, 617, 171
- Ballo, L., et al. 2007, *ApJ*, 667, 97
- Baskin, A., & Laor, A. 2005, *MNRAS*, 356, 1029
- Becker, R. H., White, R. L., & Helfand, D. J. 1995, *ApJ*, 450, 559
- Bentz, M. C., et al. 2007, *ApJ*, 662, 205
- Bentz, M. C., Peterson, B. M., Pogge, R. W., Vestergaard, M., & Onken, C. A. 2006, *ApJ*, 644, 133
- Blandford, R. D., & McKee, C. F. 1982, *ApJ*, 255, 419
- Blanton, M. R., et al. 2003, *AJ*, 125, 2276
- Boroson, T. A., & Green, R. F. 1992, *ApJS*, 80, 109
- Cannon, R., et al. 2006, *MNRAS*, 372, 425
- Collin, S., Kawaguchi, T., Peterson, B. M., & Vestergaard, M. 2006, *A&A*, 456, 75
- Croom, S. M., Smith, R. J., Boyle, B. J., Shanks, T., Miller, L., Outram, P. J., & Loaring, N. S. 2004, *MNRAS*, 349, 1397
- da Ângela, J., et al. 2007, submitted, astro-ph/0612401
- Davies, R. I., et al. 2006, *ApJ*, 646, 754
- Di Matteo, T., Springel, V., & Hernquist, L. 2005, *Nature*, 433, 604
- Dietrich, M., & Hamann, F. 2004, *ApJ*, 611, 761
- Eddington, A. S. 1913, *MNRAS*, 73, 359
- Elvis, M. 2000, *ApJ*, 545, 63
- Elvis, M., et al. 1994, *ApJS*, 95, 1
- Ferrarese, L. 2002, *ApJ*, 578, 90
- Ferrarese, L., & Merritt, D. 2000, *ApJ*, 539, L9
- Ferrarese, L., et al. 2001, *ApJ*, 555, L79
- Fine, S. et al. 2006, *MNRAS*, 373, 613
- Fukugita, M., et al. 1996, *AJ*, 111, 1748
- Gallagher, S. C., Richards, G. T., Hall, P. B., Brandt, W. N., Schneider, D. P., & Vanden Berk, D. E. 2005, *AJ*, 129, 567
- Ganguly, R., Brotherton, M. S., Cales, S., Scoggins, B., Shang, Z., Vestergaard, M. 2007, *ApJ*, 665, 990
- Gaskell, C. M. 1982, *ApJ*, 263, 79
- Gebhardt, K., et al. 2000a, *ApJ*, 539, L13
- Gebhardt, K., et al. 2000b, *ApJ*, 543, L5
- Green, R. F., Schmidt, M., & Liebert J. 1986, *ApJS*, 61, 305
- Greene, J. E., & Ho, L. C. 2005, *ApJ*, 630, 122
- Greene, J. E., & Ho, L. C. 2006, *ApJ*, 641, L21
- Greene, J. E., & Ho, L. C. 2007, *ApJ*, 667, 131
- Gunn, J. E., et al. 1998, *AJ*, 116, 3040
- Gunn, J. E., et al. 2006, *AJ*, 131, 2332
- Hao, L., et al. 2005, *AJ*, 129, 1783
- Ho, L. C. 2002, *ApJ*, 564, 120
- Hogg, D. W., Finkbeiner, D. P., Schlegel, D. J., & Gunn, J. E. 2001, *AJ*, 122, 2129
- Hopkins, P. F., Hernquist, L., Cox, T. J., Di Matteo, T., Robertson, B., & Springel, V. 2006, *ApJS*, 163, 1
- Hopkins, P. F., Richards, G. T., & Hernquist, L. 2007, *ApJ*, 654, 731
- Ivezić, Z., et al. 2004, *AN*, 325, 583
- Jiang, L. et al. 2007a, *AJ*, 134, 1150
- Jiang, L. et al. 2007b, *ApJ*, 656, 680
- Kaspi, S., Brandt, W. N., Maoz, D., Netzer, H., Schneider, D. P., & Shemmer, O. 2007, *ApJ*, 659, 997
- Kaspi, S., Maoz, D., Netzer, H., Peterson, B. M., Vestergaard, M., & Jannuzi, B. T. 2005, *ApJ*, 629, 61
- Kaspi, S., Smith, P. S., Netzer, H., Maoz, D., Jannuzi, B. T., & Giveon, U. 2000, *ApJ*, 533, 631
- Kauffmann, G., & Haehnelt, M. 2000, *MNRAS*, 311, 576
- Kelly, B. C., & Bechtold, J. 2007, *ApJS*, 168, 1
- Kochanek, C. S., Eisenstein, D., Caldwell, N., Cool, R., & Green, P. 2004, *BAAS*, 205, 9402
- Kollmeier, J. A., et al. 2006, *ApJ*, 648, 128
- Kormendy, J., & Richstone, D. 1995, *ARA&A*, 33, 581
- Krolik, J. H. 2001, *ApJ*, 551, 72
- Kurk, J. D., et al. 2007, *ApJ*, 669, 32
- Lauer, T. R., et al. 2007a, *ApJ*, 662, 808
- Lauer, T. R., Tremaine, S., Richstone, D., & Faber, S. M. 2007b, *ApJ*, 670, 249
- Lidz, A., Hopkins, P. F., Cox, T. J., Hernquist, L., & Robertson, B. 2006, *ApJ*, 641, 41
- Lupton, R., Gunn, J. E., Ivezić, Z., Knapp, G. R., & Kent, S. 2001, ASP Conference Proceedings, 238, 269
- Lynden-Bell, D. 1969, *Nature*, 223, 690
- Lynden-Bell, D., et al. 1988, *ApJ*, 326, 19
- Magorrian, J., et al. 1998, *AJ*, 115, 2285
- Malmquist, K. G. 1922, *Lund Medd. Ser. I*, 100, 1
- Marconi, A., Risaliti, G., Gilli, R., Hunt, L. K., Maiolino, R., & Salvati, M. 2004, *MNRAS*, 351, 169
- Marziani, P., Sulentic, J. W., Dultzin-Hacyan, D., Calvani, M., & Moles, M. 1996, *ApJS*, 104, 37
- McLure, R. J., & Dunlop, J. S. 2004, *MNRAS*, 352, 1390
- McLure, R. J., & Jarvis, M. J. 2002, *MNRAS*, 337, 109
- McLure, R. J., & Jarvis, M. J. 2004, *MNRAS*, 353, L45
- Merloni, A. 2004, *MNRAS*, 353, 1035
- Murray, N., Chiang, J., Grossman, S. A., & Voit, G. M. 1995, *ApJ*, 451, 498
- Nelson, C. H., Green, R. F., Bower, G., Gebhardt, K., & Weistrop, D. 2004, *ApJ*, 615, 652
- Netzer, H., Lira, P., Trakhtenbrot, B., Shemmer, O., & Cury, I. 2007, *ApJ*, in press (arXiv: 0708.3787)
- Onken, C. A., et al. 2004, *ApJ*, 615, 645
- Onken, C. A., et al. 2007, *ApJ*, in press (arXiv: 0708.1196)
- Panessa, F., et al. 2006, *A&A*, 455, 173
- Peterson, B. M. 1993, *PASP*, 105, 247
- Peterson, B. M., et al. 2004, *ApJ*, 613, 682
- Peterson, B. M. & Wandel, A. 2000, *ApJ*, 540, L13
- Pier, J. R., et al. 2003, *AJ*, 125, 1559
- Proga, D., Stone, J. M., & Kallman, T. R. 2000, *ApJ*, 543, 686
- Reichard, T. A., et al. 2003, *AJ*, 126, 2594
- Richards, G. T., 2006, preprint, astro-ph/0603827
- Richards, G. T., et al. 2002a, *AJ*, 123, 2945
- Richards, G. T., et al. 2002b, *AJ*, 124, 1
- Richards, G. T., et al. 2006a, *AJ*, 131, 2766
- Richards, G. T., et al. 2006b, *ApJS*, 166, 470
- Richstone, D., et al. 1998, *Nature*, 395, 14
- Salpeter, E. E. 1964, *ApJ*, 140, 796
- Salucci, P., Szuszkiewicz, E., Monaco, P., & Danese, L. 1999, *MNRAS*, 307, 637
- Salviander, S., Shields, G. A., Gebhardt, K., & Bonning, E. W. 2007, *ApJ*, 662, 131
- Schmidt, M., & Green, R. F. 1983, *ApJ*, 269, 352
- Schlegel, D. J., Finkbeiner, D. P., & Davis, M. 1998, *ApJ*, 500, 525
- Schneider, D. P., et al. 2003, *AJ*, 126, 2579
- Schneider, D. P., et al. 2005, *AJ*, 130, 367
- Schneider, D. P., et al. 2007, *AJ*, 134, 102
- Shen, Y., et al. 2007, *AJ*, 133, 2222
- Shen, Y., Strauss, M. A., Hall, P. B., Schneider, D. P., York, D. G., & Bahcall, N. A. 2008, *ApJ*, in press (arXiv:0712.2042)
- Silk, J., & Rees, M. J. 1998, *A&A*, 331, L1
- Smith, J. A., et al. 2002, *AJ*, 123, 2121
- Sołtan, A., 1982, *MNRAS*, 200, 115
- Spergel, D. N., et al. 2007, *ApJS*, 170, 377
- Stoughton, C., et al. 2002, *AJ*, 123, 485
- Sulentic, J. W., et al. 2006, *A&A*, 456, 929
- Sulentic, J. W., Bachev, R., Marziani, P., Negrete, C. A., & Dultzin D. 2007, *ApJ*, 666, 757
- Sulentic, J. W., Marziani, P., & Dultzin-Hacyan, D. 2000, *ARA&A*, 38, 521
- Treister, E., et al. 2006, *ApJ*, 640, 603
- Tremaine, S., et al. 2002, *ApJ*, 574, 740
- Trump, J. R., et al. 2006, *ApJS*, 165, 1
- Tucker, D. L., et al. 2006, *AN*, 327, 821
- Tundo, E., Bernardi, M., Hyde, J. B., Sheth, R. K., & Pizzella, A. 2007, *ApJ*, 663, 53
- Tytler, D., & Fan, X. 1992, *ApJS*, 79, 1
- Vanden Berk, D. E., et al. 2001, *AJ*, 122, 549
- Vestergaard, M. 2002, *ApJ*, 571, 733
- Vestergaard, M. 2004, *ApJ*, 601, 676
- Vestergaard, M., & Peterson, B. M. 2006, *ApJ*, 641, 689
- Vestergaard, M., & Wilkes, B. J. 2001, *ApJS*, 134, 1
- Weymann, R. J., Morris, S. L., Foltz, C. B., & Hewett, P. C. 1991, *ApJ*, 373, 23
- Woo, J.-H., & Urry, C. M. 2002, *ApJ*, 579, 530
- Wu, X.-B., Wang, R., Kong, M. Z., Liu, F. K., & Han, J. L. 2004, *A&A*, 424, 793
- Wyithe, J. S. B., & Loeb, A. 2003, *ApJ*, 595, 614
- Voges, W., et al. 1999, *A&A*, 349, 389
- Yip, C. W., et al. 2004, *AJ*, 128, 2603
- York, D. G., et al. 2000, *AJ*, 120, 1579

Yu, Q., & Tremaine, S. 2002, MNRAS, 335, 965

Zakamska, N. et al. 2003, AJ, 126, 2125

Zel'dovich, Y. B., & Novikov, I. D. 1964, Dokl. Akad. Nauk SSSR, 158, 811